Deep-OSG: A deep learning approach for approximating a family of operators in semigroup to model unknown autonomous systems

Junfeng Chen[a], Kailiang Wu[a,b,c,*]

[a]*Department of Mathematics, Southern University of Science and Technology, Shenzhen 518055, China*
[b]*SUSTech International Center for Mathematics, Southern University of Science and Technology, Shenzhen 518055, China*
[c]*National Center for Applied Mathematics Shenzhen (NCAMS), Shenzhen 518055, China*

ABSTRACT

This paper proposes a novel deep learning approach for approximating evolution operators and modeling unknown autonomous dynamical systems using time series data collected at varied time lags. It is a sequel to the previous works [T. Qin, K. Wu, and D. Xiu, *J. Comput. Phys.*, 395:620–635, 2019], [K. Wu and D. Xiu, *J. Comput. Phys.*, 408:109307, 2020], and [Z. Chen, V. Churchill, K. Wu, and D. Xiu, *J. Comput. Phys.*, 449:110782, 2022], which focused on learning single evolution operator with a fixed time step. This paper aims to learn a family of evolution operators with variable time steps, which constitute a semigroup for an autonomous system. The semigroup property is very crucial and links the system's evolutionary behaviors across varying time scales, but it was not considered in the previous works. We propose for the first time a framework of embedding the semigroup property into the data-driven learning process, through a novel neural network architecture and new loss functions. The framework is very feasible, can be combined with any suitable neural networks, and is applicable to learning general autonomous ODEs and PDEs. We present the rigorous error estimates and variance analysis to understand the prediction accuracy and robustness of our approach, showing the remarkable advantages of semigroup awareness in our model. Moreover, our approach allows one to arbitrarily choose the time steps for prediction and ensures that the predicted results are well self-matched and consistent. Extensive numerical experiments demonstrate that embedding the semigroup property notably reduces the data dependency of deep learning models and greatly improves the accuracy, robustness, and stability for long-time prediction.

1. Introduction

Ordinary differential equations (ODEs) and partial differential equations (PDEs) have important applications in understanding the laws of nature and modeling complicated dynamic processes in various fields of science and engineering. Many fundamental laws in physics are described by time-dependent differential equations, for example, the Maxwell equations in electromagnetics, the Navier–Stokes equations in fluid dynamics, and the Schrödinger equation in quantum mechanics. Existing differential equations are mostly derived from fundamental physical principles based on established human knowledge. However, for many practical problems, their governing equations remain unknown

---

[*]Corresponding author.
  e-mail: chenjf2@sustech.edu.cn (Junfeng Chen), wukl@sustech.edu.cn (Kailiang Wu)

due to their complex mechanisms. The fusion of artificial intelligence and data science is opening a new paradigm for modeling/evolving unknown differential equations or discovering hidden models/equations from measurement data, which has attracted extensive attention in recent years.

Unlike the traditional approach discovering new equations by derivation, data-driven modeling of governing equations tries to learn the underlying unknown dynamics or laws directly from the observed data. Earlier attempts in this direction can be found in [1, 2], which were based on comparing the numerical differentiation of experimental data with the analytic derivatives of candidate functions and then applying symbolic regression to discover nonlinear dynamical systems. A more recent approach endeavors to identify the terms in unknown governing equations from an *a priori* dictionary, which includes all possible terms that could exist in the underlying equations; see e.g. [3, 4]. Classic methods along this approach typically use certain sparsity-promoting algorithms, such as LASSO [5] and compressed sensing [6, 7], to construct parsimonious models from a large set of dictionary encompassing all potential models; cf. [3, 8, 9, 4, 10]. Besides, many machine learning techniques, particularly deep learning, have been developed to discover the forms of governing equations; see, for example, [11, 12, 13, 14, 15, 16, 17]. There are also some recent efforts (e.g. [18, 19]) aiming to eliminate the requirement of specifying *a prior* dictionary of all potential terms in the underlying equations. For more developments, the readers are also referred to some related works based on Gaussian process regression [20], model selection [21], Koopman theory [22], classical polynomial approximation [23, 24], linear multistep methods [25], genetic algorithms [26, 27, 28], and the references therein.

Recently, another (different) approach for data-driven modeling of unknown dynamical systems was systematically proposed in a series of papers [29, 30, 31]. Instead of identifying the terms in the unknown governing equations, this new approach focuses on approximating the *evolution operator* (also called *flow map*) of the underlying equations. For an autonomous system, its evolution operator completely describes the system's dynamics over time. Consequently, the evolution operator, once successfully learned, can be recursively employed to predict the solution behavior of the unknown dynamical system in the future [29, 30, 31]. Although this approach does not aim to directly recover the exact form of the equations, it is indeed equivalent to recovering some integral form of the underlying equations [29, 30]. This approach avoids the need for numerical approximation of time derivatives (which is difficult to obtain and may be subject to large error especially for noisy data) and allows larger time steps during the learning and prediction process. Moreover, the approach based on learning evolution operators does not require a-priori knowledge about all potential terms in the unknown governing equations. While the approach of recovering equations should be coupled with appropriate numerical schemes to further solve the learned equations for system predictions, the learned evolution operator can be directly used to perform predictions. The effectiveness of the evolution-operator-based approach has been demonstrated for learning ODEs [29], modeling PDEs in both generalized Fourier spaces [30] and nodal space [31]. In more recent works, this approach has also been extended to data-driven modeling of parametric differential equations [32], partially observed systems [33, 34], non-autonomous systems [35], model correction [36], and biological models [37]. These advancements demonstrate the applicability and potential of this approach in various fields.

More recently, deep learning techniques have also been developed for approximating general operators which are maps between two infinite-dimensional function spaces, such as integrals, the Laplace transform, and the solution operators of differential equations. The related works in this direction include but are not limited to DeepONet [38, 39, 40], neural operator [41], multipole graph neural operator [42], Fourier neural operator (FNO) [43], Markov neural operator [44], and nonlocal kernel network [45], etc.

This paper aims to develop a novel deep learning approach for approximating a family of evolution operators in semigroup, with applications to data-driven modeling of unknown autonomous ODE and PDE systems. Unlike the previous works [29, 30, 31] which focused on learning a single evolution operator with a constant time step, our new approach aims to learn a family of evolution operators with variable time steps. This allows us to model unknown autonomous dynamical systems from time series data collected at varied time lags. For an autonomous system, all the evolution operators with different time lags constitute a one-parameter *semigroup* in mathematics. The semigroup property is very crucial, as it links the system's evolutionary behaviors across varying time scales. However, such an important property has not been taken into account in the previous methods developed in [29, 30, 31]. The main objective of this work is to carefully embed the semigroup property into the data-driven learning

process, yielding the semigroup-informed models that demonstrate improved performance in terms of robustness and reduced error accumulation over time, in comparison with the purely data-driven approach. The contribution, novelty, and significance of this paper are outlined as follows:

- We present a new framework for learning evolution operators and modeling unknown ODEs and PDEs using data. The framework incorporates the evolution time as an input feature in deep neural networks, enabling the learning of a family of evolution operators from observed data with varied time steps, rather than a single evolution operator defined by a fixed time step. Most notably, we carefully embed the semigroup property of the evolution operators into our framework. The framework produces data-driven models continuous in time and allows one to perform long-time predictions with arbitrary evolution time steps from any given initial states.

- In order to effectively embed the semigroup property, we design a new residual network architecture for our framework. Besides adding the initial state to the output layer, we propose a second skip connection for the time step, by multiplying it with the network's output layer. The new architecture strictly enforces a desired semigroup constraint such that the neural network model degenerates to the identity map if the time stepsize reduces to zero.

- We derive a novel loss function combining the vanilla fitting loss with a regularization term informed by the semigroup property. Through comparisons by extensive numerical experiments, we construct a highly effective semigroup-informed regularization term, which does not depend on the observed data. Instead, the regularization term is carefully designed based on semigroup residues calculated by randomly generated initial states and time lags, thereby effectively enforcing the semigroup property on the entire domain of interest. The semigroup awareness in our model significantly improves the prediction accuracy, and greatly enhances the robustness and stability of long-time prediction. Moreover, our model allows one to arbitrarily choose the time steps for prediction, and ensures that the predicted results are well self-matched and consistent for different partitions of the time interval.

- We carry out the rigorous error estimates and variance analysis to understand the prediction accuracy and robustness of our method.

- It is worth mentioning the general flexibility of our framework. First, since our network architecture and semigroup-informed loss function are non-intrusive to the basic network structures, the framework is very feasible and can be combined with any suitable neural networks including fully-connected neural networks (FNNs), convolutional neural networks, locally connected networks, and FNO, etc. In our numerical experiments, we implement the combinations of our framework with various neural networks. Secondly, our framework is applicable to a wide range of autonomous ODEs and PDEs. We will first present the framework on learning unknown ODEs and then extend it to modeling unknown PDEs in either modal or nodal space.

- We present extensive numerical experiments on various ODEs and PDEs to demonstrate the effectiveness of our method. These include a highly stiff ODE system to show that our model is able to accurately capture the multiscale dynamics in long-time prediction. Interestingly, we observe that our data-driven method, although resembling an explicit algorithm, allows a very large time step even for very stiff problems. We also present a challenging example on modeling the Navier–Stokes equations. The numerical results validate the good stability and robustness of our semigroup-informed method in long-time prediction.

Notice that adequate amount of data was used in the previous works [29, 30, 31]. For example, tens of thousands data pairs were used in learning ODEs [29], and hundreds of thousands data were employed in modeling PDEs in [30]. However, in practice, collecting measurement data from real-world systems can be very costly or difficult due to some resource constraints or limited experimental accessibility. In the present paper, we shall assume that the measurement data can be very limited. In this case, we find embedding the semigroup constraint is very helpful or even essential to avoid over-fitting and notably reduce the required data, as the semigroup-informed loss function plays an important role of regularization.

The remainder of this article is organized as follows. After the basic setup in section 2, we present the deep learning framework for learning evolution operators in semigroup for autonomous ODEs in Section 3. The framework is extended to modeling PDEs in Section 4. Several numerical experiments are presented in Section 5, before concluding the paper in Section 6.

2. Setup and preliminaries

We consider a set of state variables $\boldsymbol{u} \in \mathbb{R}^n$, which are governed by an *unknown* autonomous time-dependent differential system. Assume that the state variables $\boldsymbol{u}$ are measurable or observable, namely, the measurement data of $\boldsymbol{u}$ are available. We aim to seek accurate data-driven modeling of the unknown autonomous system and construct an accurate predicting model for the unknown dynamics based on the state variable data.

For the sake of convenience, we first consider the ODE case that the underlying unknown governing equations are autonomous ODEs

$$\frac{d\boldsymbol{u}}{dt} = \boldsymbol{f}(\boldsymbol{u}), \quad \boldsymbol{u}(t_0) = \boldsymbol{u}_0 \tag{1}$$

with $\boldsymbol{f} : \mathbb{R}^n \to \mathbb{R}^n$ being unknown, while the extension of our discussions to the PDE case will be studied in Section 4. Assume that the measurement data of $\boldsymbol{u}$ are collected along a number of different trajectories. Let $t_0 < t_1 < \cdots < t_K$ be a sequence of time instances. We use

$$\boldsymbol{u}_k^{(i)} = \boldsymbol{u}(t_k; \boldsymbol{u}_0^{(i)}, t_0) + \boldsymbol{\epsilon}_k^{(i)}, \qquad k = 1, \ldots, K_i, \quad i = 1, \ldots, I_{traj} \tag{2}$$

to denote the solution state measured at the time instance t_k along the i-th trajectory originated from the initial state $\boldsymbol{u}_0^{(i)}$ at t_0, for a total number of I_{traj} trajectories. In practice, the data may contain some measurement noises $\boldsymbol{\epsilon}_k^{(i)}$, which are usually modeled as random variables.

2.1. Evolution operator

While many of the existing work seek to directly learn the right-hand-side term $\boldsymbol{f}$ of the governing equations, we here adopt a different approach which seeks to approximate the evolution operator of the underlying equations. The idea of this approach was proposed in [29] for modeling unknown ODEs and further developed in [30, 31] for modeling unknown PDEs.

An evolution operator $\boldsymbol{\Phi}_\Delta : \mathbb{R}^n \to \mathbb{R}^n$, which is sometimes also called *flow map* in the ODE community, describes the evolution of state variables from time t_0 to time $t_0 + \Delta$. It can be defined through the integral form of equations (1) as follows

$$\boldsymbol{\Phi}_\Delta(\boldsymbol{u}_0) := \boldsymbol{u}(t_0 + \Delta; \boldsymbol{u}_0, t_0) = \boldsymbol{u}_0 + \int_{t_0}^{t_0+\Delta} \boldsymbol{f}(\boldsymbol{u}(s)) \mathrm{d}s = [\mathbf{I}_n + \Delta\boldsymbol{\phi}(\cdot, \Delta)](\boldsymbol{u}_0), \tag{3}$$

where $\mathbf{I}_n$ is the identity matrix of size $n \times n$, and for any $\boldsymbol{u} \in \mathbb{R}^n$,

$$\boldsymbol{\phi}(\cdot, \Delta)[\boldsymbol{u}] = \boldsymbol{\phi}(\boldsymbol{u}, \Delta) = \frac{1}{\Delta} \int_0^\Delta \boldsymbol{f}(\boldsymbol{\Phi}_s(\boldsymbol{u})) \mathrm{d}s = \boldsymbol{f}(\boldsymbol{\Phi}_\tau(\boldsymbol{u})) \tag{4}$$

denotes the time-averaged increment, where the mean value theorem is used with some $\tau \in [0, \Delta]$.

For autonomous systems, the evolution operator completely determines the evolution of the solution from one state to another state at a future time. Learning the evolution operator from data allows us to conduct prediction of the system via recursively using the learned evolution operator.

2.2. Semigroup property

For an autonomous system (1), all the evolution operators $\{\boldsymbol{\Phi}_\Delta\}_{\Delta \geq 0}$ constitute a one-parameter *semigroup*, namely, they satisfy

$$\boldsymbol{\Phi}_0 = \mathbf{I}_n, \tag{5a}$$

$$\boldsymbol{\Phi}_{\Delta_1 + \Delta_2} = \boldsymbol{\Phi}_{\Delta_1} \circ \boldsymbol{\Phi}_{\Delta_2} \quad \forall \Delta_1, \Delta_2 \in \mathbb{R}^+. \tag{5b}$$

The first constraint (5a) requires the evolution operator to be the identity map when the time step $\Delta = 0$, which is natural for time-dependent differential equations. The second constraint (5b) distinguishes the forward dynamics of autonomous systems from non-autonomous ones, and it connects the system evolution behaviors at different time scales.

Instead of learning a single evolution operator with a fixed time step Δ as in [29, 30], in the present paper we aim to establish a new numerical framework for learning a family of evolution operators $\{\mathbf{\Phi}_\Delta\}_{\Delta \geq 0}$ with variable time steps $\Delta \in [0, T]$ and especially embedding the semigroup property (5) into the learning process.

2.3. Data reorganization

In order to learn the evolution operator with the semigroup property (5) embedded, we reorganize the data (2) into several groups, and each group has three samples at neighboring time instances separated by two time lags $\Delta_k := t_{k+1} - t_k$ and $\Delta_{k+1} := t_{k+2} - t_{k+1}$, as follows

$$\left\{ \boldsymbol{u}_k^{(i)}, \boldsymbol{u}_{k+1}^{(i)}, \boldsymbol{u}_{k+2}^{(i)} \right\}, \qquad k = 1, \ldots, K_i - 2, \quad i = 1, \ldots, I_{traj}.$$

Note that for autonomous systems, the time variable t can be arbitrarily shifted and only the time difference Δ is relevant. Hence, for notational convenience, we denote the entire data set as

$$\left\{ \boldsymbol{u}_{0,j}, \ \Delta_{1,j}, \ \boldsymbol{u}_{1,j}, \ \Delta_{2,j}, \ \boldsymbol{u}_{3,j} \right\}_{j=1}^{J} \tag{6}$$

with $J = \sum_{i=1}^{I_{traj}} (K_i - 2)$ is the total number of data groups. If the data are noiseless, we have the following relations

$$\boldsymbol{u}_{1,j} = \mathbf{\Phi}_{\Delta_{1,j}}(\boldsymbol{u}_{0,j}), \quad \boldsymbol{u}_{2,j} = \mathbf{\Phi}_{\Delta_{2,j}}(\boldsymbol{u}_{1,j}), \quad \boldsymbol{u}_{2,j} = \mathbf{\Phi}_{\Delta_{1,j}+\Delta_{2,j}}(\boldsymbol{u}_{0,j}).$$

3. Deep-OSG approach for evolution operator learning

In this section, we present the deep learning approach, termed as Deep-OSG, for approximating a family of evolution operators with semigroup property (5).

3.1. A modified ResNet architecture: OSG-Net

3.1.1. ResNet

As shown in [29, 30], the residual network (ResNet) is particularly suitable for learning an evolution operator with a fixed time lag. The notion of ResNet [46] is to explicitly introduce the identity mapping in the network and force the neural network to effectively learn the residue of the input-output mapping. The illustration of a one-step ResNet is provided in Fig. 1a. Mathematically, a ResNet based on fully connected feedforward deep neural network may be expressed as

$$\boldsymbol{u}_{out} = \mathbf{N}_{\boldsymbol{\theta}}(\boldsymbol{u}_{in}) = \boldsymbol{u}_{in} + \mathcal{N}_{\boldsymbol{\theta}}(\boldsymbol{u}_{in}) = (\mathbf{I}_n + \mathcal{N}_{\boldsymbol{\theta}})(\boldsymbol{u}_{in}), \tag{7}$$

where $\boldsymbol{u}_{in}$ denotes the network input, $\boldsymbol{u}_{out}$ is the network output, $\boldsymbol{\theta}$ denotes all the trainable parameters in the neural network, and

$$\mathcal{N}_{\boldsymbol{\theta}}(\boldsymbol{u}_{in}) = \mathbf{W}_{L+1} \circ (\sigma_L \circ \mathbf{W}_L) \circ \cdots \circ (\sigma_1 \circ \mathbf{W}_1)(\boldsymbol{u}_{in})$$

denotes a fully connected feedforward neural network (FNN) of L hidden layers, with $\mathbf{W}_j$ being the weight matrix between the jth layer and the $(j+1)$th layer, σ_j denoting the activation function, and $\circ$ being the composition operator. Multiple ResNet blocks can be stacked recursively, providing a deeper recursive ResNet architecture (see Figure 1c). Mathematically, a multi-step recursive ResNet structure can be formulated as

$$\mathbf{N}_{\boldsymbol{\theta}} = (\mathbf{I}_n + \mathcal{N}_{\boldsymbol{\theta}_K}) \circ \cdots \circ (\mathbf{I}_n + \mathcal{N}_{\boldsymbol{\theta}_1}),$$

where K is the number of ResNet blocks, and $\boldsymbol{\theta}_i$ is the network parameters in the ith block. The recursive ResNet enables the network to learn dynamics at smaller time scales than the time stepsize of the collected samples and is thus more advantageous than a single step ResNet for evolution operator learning [29].

5

When the time lag Δ in the data is a constant, the ResNet structure (7) is particularly suitable for approximating the evolution operator $\mathbf{\Phi}_\Delta$. By comparing (3) with (7), one can see that the FNN operator $\mathcal{N}_\theta$ becomes an approximation to the effective increment $\int_0^\Delta \boldsymbol{f}(\mathbf{\Phi}_s(\boldsymbol{u}))\mathrm{d}s$. However, the network architecture (7) does not include the time step as its input and thus is not applicable for data collected with varied time lags. Moreover, the effective increment $\int_0^\Delta \boldsymbol{f}(\mathbf{\Phi}_s(\boldsymbol{u}))\mathrm{d}s = O(\Delta)$ approaches zero as $\Delta \to 0$, which is, however, not accommodated by the ResNet structure (7).

(a) ResNet for trajectories with constant time step.

(b) OSG-Net for trajectories with changing time step.

(c) Recursive ResNets applicable to trajectories with fixed time step. Each block is a ResNet as described in Figure 1a. We set $K = 2$ for illustration.

(d) Recursive OSG-Net applicable to trajectories with changing time step. Each block is an OSG-Net described in Figure 1b. The time step Δ is divided by K and fed to each block. We set $K = 2$ for illustration.
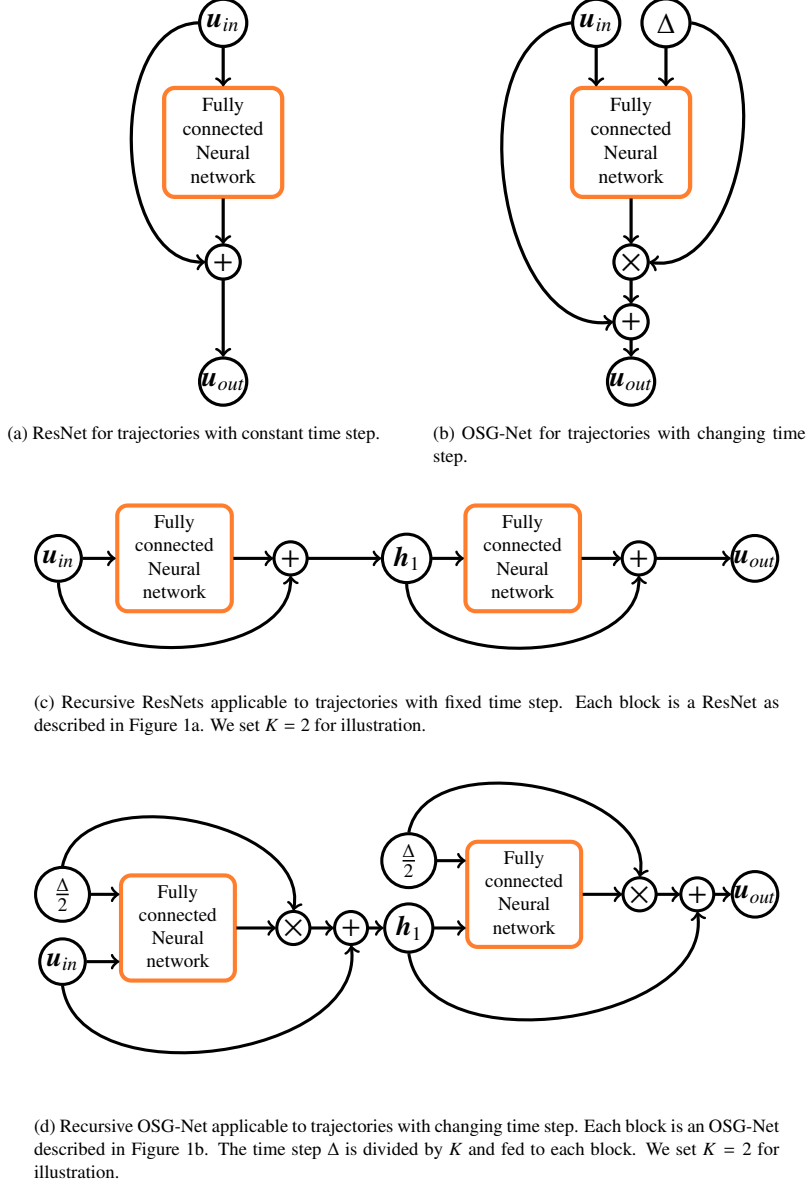
Fig. 1: **Residual neural networks (ResNets) for flow map learning**.

3.1.2. OSG-Net

To address the above-mentioned limitations of ResNet, we propose a modified ResNet architecture

$$\boldsymbol{u}_{out} = \mathbf{N}_\theta(\boldsymbol{u}_{in}, \Delta) = \boldsymbol{u}_{in} + \Delta\mathcal{N}_\theta(\boldsymbol{u}_{in}, \Delta), \tag{8}$$

which is called operator semigroup network (OSG-Net) as it naturally incorporates the first semigroup property (5) of the evolution operator. The OSG-Net architecture (8) is illustrated in Figure 1b, where the initial state variables $\boldsymbol{u}_{in}$

and the evolution time Δ are concatenated before being fed into the network $\mathcal{N}_\theta$. Compared to Figure 1a, we introduce a second skip connection which multiplies Δ with the output of $\mathcal{N}_\theta$. Such a new design makes the whole architecture continuously reduce to an identity map as $\Delta \to 0$, thereby strictly enforcing the property (5a). By comparing (3) with (8), we see that the OSG-Net architecture matches the formula $\Phi_\Delta(\boldsymbol{u}_0) = [\mathbf{I}_n + \Delta\boldsymbol{\phi}(\cdot, \Delta)](\boldsymbol{u}_0)$, and the FNN operator $\mathcal{N}_\theta$ becomes an approximation to the time-averaged effective increment $\boldsymbol{\phi}(\cdot, \Delta)$, namely,

$$\mathcal{N}_\theta(\boldsymbol{u}, \Delta) \approx \boldsymbol{\phi}(\boldsymbol{u}, \Delta) = \frac{1}{\Delta}\int_0^\Delta \boldsymbol{f}(\Phi_s(\boldsymbol{u}))\mathrm{d}s. \tag{9}$$

Similar to the recursive ResNet in Figure 1c, we can also propose deep recursive OSG-Net architectures. To do this, we devide the time lag Δ by K, with K being the total number of blocks (see Figure 1d). The time-step input of each OSG-Net block is Δ/K. Mathematically, a multi-step recursive OSG-Net structure can be formulated as

$$\mathbf{N}_\theta = \left[\mathbf{I}_n + \frac{\Delta}{K}\mathcal{N}_{\theta_K}\left(\cdot, \frac{\Delta}{K}\right)\right] \circ \cdots \circ \left[\mathbf{I}_n + \frac{\Delta}{K}\mathcal{N}_{\theta_1}\left(\cdot, \frac{\Delta}{K}\right)\right],$$

where K is the number of OSG-Net blocks, and $\boldsymbol{\theta}_i$ is the network parameters in the ith block. In such a stacked architecture, each OSG-Net block is expected to learn dynamics at smaller time scales. A study on the number of blocks will be conducted in Section 5.2.1.

Remark 1. The proposed OSG-Net architecture is very feasible: it can be combined with other suitable basic networks, such as convolution neural networks and locally connected networks, in addition to FNN. In fact, such an architecture can also be combined with other suitable approximators, e.g. polynomials.

Remark 2 (Multiscale stepsizes)**.** In the multiscale problems (such as the chemical reaction problem of Robertson, which will be simulated in Section 5.1.4), the time stepsize Δ may vary from a small scale such as 10^{-5} to a large scale such as 1 or 10. In such cases, we propose a slightly modified multiscale version of the OSG-Net architecture

$$\boldsymbol{u}_{out} = \mathbf{N}_\theta(\boldsymbol{u}_{in}, \Delta) = \boldsymbol{u}_{in} + \Delta\mathcal{N}_\theta(\boldsymbol{u}_{in}, -\log_{10}\Delta), \tag{10}$$

which we find is quite effective to model the multiscale evolution structures of the underlying system over time; see Section 5.1.4.

3.2. Semigroup-informed learning

The proposed OSG-Net is trained by minimizing suitable loss function. In the purely data-driven case, the conventional loss function is

$$L(\boldsymbol{\theta}) = \frac{1}{J}\sum_{j=1}^{J} L_{data,j}(\boldsymbol{\theta}) \quad \text{with} \quad L_{data,j}(\boldsymbol{\theta}) = \frac{1}{2}\left[\ell\left(\boldsymbol{u}_{1,j}, \widehat{\boldsymbol{u}}_{01,j}(\boldsymbol{\theta})\right) + \ell\left(\boldsymbol{u}_{2,j}, \widehat{\boldsymbol{u}}_{12,j}(\boldsymbol{\theta})\right)\right], \tag{11}$$

where

$$\widehat{\boldsymbol{u}}_{01,j}(\boldsymbol{\theta}) := \mathbf{N}_\theta(\boldsymbol{u}_{0,j}, \Delta_{1,j}) \quad \text{and} \quad \widehat{\boldsymbol{u}}_{12,j}(\boldsymbol{\theta}) := \mathbf{N}_\theta(\boldsymbol{u}_{1,j}, \Delta_{2,j})$$

are two single-step predictions given by the OSG-Net parametrized by $\boldsymbol{\theta}$. In (11), $\ell(\cdot, \cdot)$ is a "loss metric" which measures the differences between the network outputs and the data. A standard metric is based on the vector l^2 norm square, namely, $\ell(\boldsymbol{u}, \hat{\boldsymbol{u}}) = \|\boldsymbol{u} - \hat{\boldsymbol{u}}\|_2^2$. Another option is the relative l_2 norm: $\ell(\boldsymbol{u}, \hat{\boldsymbol{u}}) = \frac{\|\boldsymbol{u} - \hat{\boldsymbol{u}}\|_2}{\|\boldsymbol{u}\|_2}$ as suggested in [43].

However, neural network model based on the purely data-driven loss function (11) does not embed the second semigroup property (5b), which can be expressed as

$$\Phi_{\Delta_1 + \Delta_2}(\boldsymbol{u}_0) = \Phi_{\Delta_2}\left(\Phi_{\Delta_1}(\boldsymbol{u}_0)\right) = \Phi_{\Delta_1}\left(\Phi_{\Delta_2}(\boldsymbol{u}_0)\right) \qquad \forall \Delta_1, \Delta_2 > 0, \quad \forall \boldsymbol{u}_0 \in D, \tag{12}$$

where $D \subseteq \mathbb{R}^n$ is the domain of interest in the phase space.

Note that the identity (12) can be treated as a constraint not relying on labeled data. We propose a novel regularization method, which efficiently incorporates the semigroup property (12) into our OSG-Net model without requiring any extra measurement data.

Specifically, we introduce the following new loss function

$$L(\boldsymbol{\theta}) = \frac{1}{J} \sum_{j=1}^{J} \left(\frac{1}{1+\lambda} \left(L_{data,j}(\boldsymbol{\theta}) + \lambda L_{SG,j}(\boldsymbol{\theta}) \right) \right) \tag{13}$$

where λ is a regularization factor. The semigroup-informed loss function is defined as

$$L_{SG,j}(\boldsymbol{\theta}) := \frac{1}{2Q} \sum_{i=1}^{Q} \left[\ell \left(\widetilde{\boldsymbol{u}}_{02,ij}(\boldsymbol{\theta}), \widetilde{\boldsymbol{u}}_{012,ij}(\boldsymbol{\theta}) \right) + \ell \left(\widetilde{\boldsymbol{u}}_{02,ij}(\boldsymbol{\theta}), \widetilde{\boldsymbol{u}}_{021,ij}(\boldsymbol{\theta}) \right) \right], \tag{14}$$

where

$$\widetilde{\boldsymbol{u}}_{02,ij} = \mathbf{N}_{\boldsymbol{\theta}} \left(\widetilde{\boldsymbol{u}}_{0,ij}, \Delta_{1,ij} + \Delta_{2,ij} \right),$$

$$\widetilde{\boldsymbol{u}}_{012,ij} = \mathbf{N}_{\boldsymbol{\theta}} \left(\mathbf{N}_{\boldsymbol{\theta}} \left(\widetilde{\boldsymbol{u}}_{0,ij}, \Delta_{1,ij} \right), \Delta_{2,ij} \right),$$

$$\widetilde{\boldsymbol{u}}_{021,ij} = \mathbf{N}_{\boldsymbol{\theta}} \left(\mathbf{N}_{\boldsymbol{\theta}} \left(\widetilde{\boldsymbol{u}}_{0,ij}, \Delta_{2,ij} \right), \Delta_{1,ij} \right)$$

represent the prediction of the state at time $t = t_0 + \Delta_{1,ij} + \Delta_{2,ij}$ via three different forward passages, the "initial" state $\widetilde{\boldsymbol{u}}_{0,ij}$ is randomly sampled in D, and $\{\Delta_{1,ij}, \Delta_{2,ij}\}$ are two randomly selected time stepsizes. See Figure 2 for an illustration of the semigroup loss function (14). By minimizing (13), we expect that the trained OSG-Net model successfully embeds the semigroup property (5b).

Remark 3. Since the stepsizes $\Delta_{1,ij}$ and $\Delta_{2,ij}$ are random, it seems unnecessary to simultaneously include both $\ell \left(\widetilde{\boldsymbol{u}}_{02,ij}(\boldsymbol{\theta}), \widetilde{\boldsymbol{u}}_{012,ij}(\boldsymbol{\theta}) \right)$ and $\ell \left(\widetilde{\boldsymbol{u}}_{02,ij}(\boldsymbol{\theta}), \widetilde{\boldsymbol{u}}_{021,ij}(\boldsymbol{\theta}) \right)$ in the loss function (14). However, our numerical results demonstrate that including both of them is beneficial for training the network to enforce the semigroup property (5b).
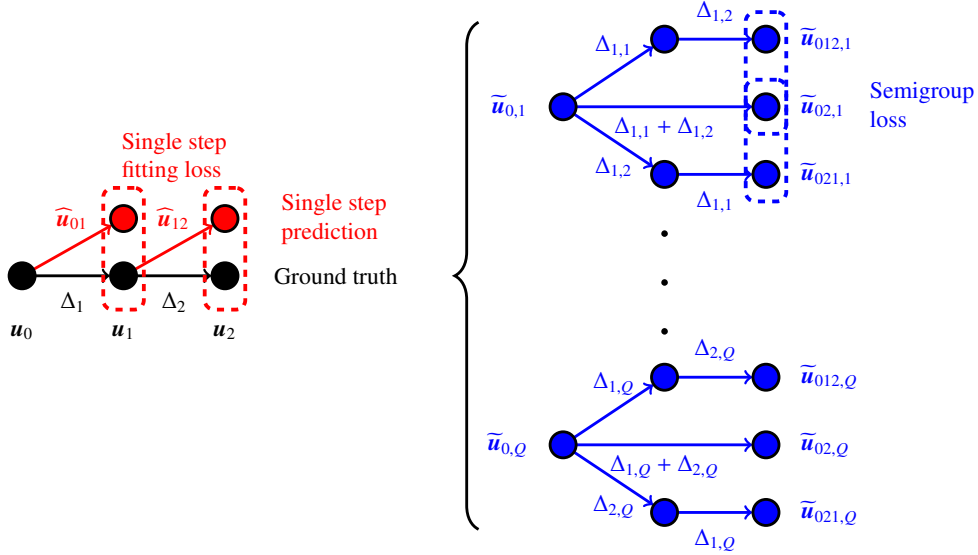

Fig. 2: **Semigroup-informed loss function**. As shown in equation (13), each observed trajectory (on the left) is grouped with Q randomly generated tuples (on the right). The semigroup residues are calculated on the tuples, so no supplementary labeled data is required.

Besides the semigroup-informed loss function (14), we also introduce another "indirect" semigroup-embedding approach, which implicitly enhances the semigroup property (5b), based on a purely data-driven two-step loss function

$$L(\boldsymbol{\theta}) = \frac{1}{J} \sum_{j=1}^{J} L_{ISG,j}(\boldsymbol{\theta}) \tag{15}$$

by adding three terms to $L_{data,j}$ as follows:

$$L_{ISG,j}(\boldsymbol{\theta}) = \frac{1}{5}\left[\ell\left(\boldsymbol{u}_{1,j}, \widehat{\boldsymbol{u}}_{01,j}(\boldsymbol{\theta})\right) + \ell\left(\boldsymbol{u}_{2,j}, \widehat{\boldsymbol{u}}_{12,j}(\boldsymbol{\theta})\right) + \ell\left(\boldsymbol{u}_{2,j}, \widehat{\boldsymbol{u}}_{02,j}(\boldsymbol{\theta})\right) + \ell\left(\boldsymbol{u}_{2,j}, \widehat{\boldsymbol{u}}_{012,j}(\boldsymbol{\theta})\right) + \ell\left(\boldsymbol{u}_2, \widehat{\boldsymbol{u}}_{021,j}(\boldsymbol{\theta})\right)\right],$$

where

$$\widehat{\boldsymbol{u}}_{02,j}(\boldsymbol{\theta}) = \mathbf{N}_{\boldsymbol{\theta}}(\boldsymbol{u}_{0,j}, \Delta_{1,j} + \Delta_{2,j}),$$
$$\widehat{\boldsymbol{u}}_{012,j}(\boldsymbol{\theta}) = \mathbf{N}_{\boldsymbol{\theta}}(\mathbf{N}_{\boldsymbol{\theta}}(\boldsymbol{u}_{0,j}, \Delta_{1,j}), \Delta_{2,j}),$$
$$\widehat{\boldsymbol{u}}_{021,j}(\boldsymbol{\theta}) = \mathbf{N}_{\boldsymbol{\theta}}(\mathbf{N}_{\boldsymbol{\theta}}(\boldsymbol{u}_{0,j}, \Delta_{2,j}), \Delta_{1,j}),$$

are three different approximations of the state $\boldsymbol{u}_{2,j}$. By minimizing (15), we expect that the trained network model satisfies $L_{ISG,j}(\boldsymbol{\theta}) \leq \epsilon$ for some small $\epsilon > 0$ so that

$$\left\|\mathbf{N}_{\boldsymbol{\theta}}(\mathbf{N}_{\boldsymbol{\theta}}(\boldsymbol{u}_{0,j}, \Delta_{1,j}), \Delta_{2,j}) - \mathbf{N}_{\boldsymbol{\theta}}(\boldsymbol{u}_{0,j}, \Delta_{1,j} + \Delta_{2,j})\right\|_2 = \left\|\widehat{\boldsymbol{u}}_{012,j}(\boldsymbol{\theta}) - \widehat{\boldsymbol{u}}_{02,j}(\boldsymbol{\theta})\right\|_2$$
$$\leq \left\|\boldsymbol{u}_{2,j} - \widehat{\boldsymbol{u}}_{012,j}(\boldsymbol{\theta})\right\|_2 + \left\|\boldsymbol{u}_{2,j} - \widehat{\boldsymbol{u}}_{02,j}(\boldsymbol{\theta})\right\|_2 \leq 2\sqrt{5\epsilon},$$
$$\left\|\mathbf{N}_{\boldsymbol{\theta}}(\mathbf{N}_{\boldsymbol{\theta}}(\boldsymbol{u}_{0,j}, \Delta_{2,j}), \Delta_{1,j}) - \mathbf{N}_{\boldsymbol{\theta}}(\boldsymbol{u}_{0,j}, \Delta_{1,j} + \Delta_{2,j})\right\|_2 = \left\|\widehat{\boldsymbol{u}}_{021,j}(\boldsymbol{\theta}) - \widehat{\boldsymbol{u}}_{02,j}(\boldsymbol{\theta})\right\|_2$$
$$\leq \left\|\boldsymbol{u}_{2,j} - \widehat{\boldsymbol{u}}_{021,j}(\boldsymbol{\theta})\right\|_2 + \left\|\boldsymbol{u}_{2,j} - \widehat{\boldsymbol{u}}_{02,j}(\boldsymbol{\theta})\right\|_2 \leq 2\sqrt{5\epsilon},$$

if the mean squared loss metric is used. Therefore, the two-step loss function (15) implicitly enforces the semigroup property (5b) along the sampling trajectories.

Remark 4. For clarity, we refer to the conventional data-driven approach (11) as the *baseline method*, we refer to our main approach based on (13) as the *global direct semigroup-informed (GDSG) method*, and we refer to the approach based on (15) as the *local indirect semigroup-informed (LISG) method*. This is because the GDSG method directly enforces the semigroup property (5b) globally over the random samples widely distributed in the entire domain D, while the LISG method indirectly enhances the semigroup property (5b) locally only along the sampling trajectories.

Remark 5 (Limited data). When adequate amount of data is available, the neural network model can be effectively trained to learn the evolution operator [29, 30]. However, in practice, collecting measurement data from real-world systems can be very costly or difficult due to resource constraints or limited experimental accessibility. When the measurement data (6) is very limited, embedding the semigroup constraint (5b) becomes very helpful or even essential to avoid over-fitting, as the semigroup-informed loss function plays an important role of regularization. It not only significantly reduces the required data and improves the deep learning accuracy but also greatly enhances the robustness and stability of long-time prediction; see Section 5.

3.3. Model prediction

Once the OSG-Net model (8) is successfully trained, we can recursively employ the model to conduct prediction for any arbitrarily given initial state $\boldsymbol{u}(t_0)$ as follows

$$\begin{cases} \boldsymbol{u}^{pre}(t_0) = \boldsymbol{u}(t_0) \\ \boldsymbol{u}^{pre}(t_{j+1}) = \boldsymbol{u}^{pre}(t_j) + \Delta_j \mathcal{N}_{\boldsymbol{\theta}}(\boldsymbol{u}^{pre}(t_j), \Delta_j), \qquad j = 0, 1, \dots \end{cases} \tag{16}$$

where $\Delta_j = t_{j+1} - t_j$.

Even though the form of the prediction model (16) resembles the first-order forward Euler method for time stepping, the model (16) is indeed an approximation of the exact (rather than first-order) time integrator, because there is no explicit discretization error in time. The only source of error in the prediction model (16) is the approximation error of the time-averaged effective increment (9).

In order to estimate a bound for the prediction error, we first introduce the following lemma.

Lemma 1. *Suppose $\boldsymbol{f}$ is Lipschitz continuous with Lipschitz constant L_f on a set $D \subseteq R^n$. For any $T > 0$, define*

$$D_T = \{\boldsymbol{u} \in D : \ \boldsymbol{\Phi}_\Delta(\boldsymbol{u}) \in D \ \forall \Delta \in [0, T]\}.$$

Then we have

$$\left\|\boldsymbol{\phi}(\boldsymbol{u}_1, \Delta) - \boldsymbol{\phi}(\boldsymbol{u}_2, \Delta)\right\|_2 \le \frac{\mathrm{e}^{L_f \Delta} - 1}{\Delta} \left\|\boldsymbol{u}_1 - \boldsymbol{u}_2\right\|_2 \qquad \forall \boldsymbol{u}_1, \boldsymbol{u}_2 \in D_T \quad \forall \Delta \in [0, T]. \tag{17}$$

Proof. Note that $\boldsymbol{\Phi}_t(u_1) = \boldsymbol{u}_1 + t\boldsymbol{\phi}(\boldsymbol{u}_1, t)$ is the solution to the ODE $\frac{du}{dt} = \boldsymbol{f}(\boldsymbol{u})$ with initial data $\boldsymbol{u}_1$. Thus, we have

$$\frac{d}{dt}\Big(t\boldsymbol{\phi}(\boldsymbol{u}_1, t)\Big) = \boldsymbol{f}(\boldsymbol{\Phi}_t(u_1)). \tag{18}$$

Similarly, we obtain

$$\frac{d}{dt}\Big(t\boldsymbol{\phi}(\boldsymbol{u}_2, t)\Big) = \boldsymbol{f}(\boldsymbol{\Phi}_t(u_2)). \tag{19}$$

Combining (18) with (19) gives

$$\frac{d}{dt}\Big(t(\boldsymbol{\phi}(\boldsymbol{u}_1, t) - \boldsymbol{\phi}(\boldsymbol{u}_2, t))\Big) = \boldsymbol{f}(\boldsymbol{\Phi}_t(u_1)) - \boldsymbol{f}(\boldsymbol{\Phi}_t(u_2)). \tag{20}$$

It follows that

$$\begin{aligned}
\frac{1}{2}\frac{d}{dt}\Big(t^2\left\|\boldsymbol{\phi}(\boldsymbol{u}_1, t) - \boldsymbol{\phi}(\boldsymbol{u}_2, t)\right\|_2^2\Big) &= \Big(t(\boldsymbol{\phi}(\boldsymbol{u}_1, t) - \boldsymbol{\phi}(\boldsymbol{u}_2, t))\Big) \cdot \frac{d}{dt}\Big(t(\boldsymbol{\phi}(\boldsymbol{u}_1, t) - \boldsymbol{\phi}(\boldsymbol{u}_2, t))\Big) \\
&= t(\boldsymbol{\phi}(\boldsymbol{u}_1, t) - \boldsymbol{\phi}(\boldsymbol{u}_2, t)) \cdot \Big(\boldsymbol{f}(\boldsymbol{\Phi}_t(u_1)) - \boldsymbol{f}(\boldsymbol{\Phi}_t(u_2))\Big) \\
&\le t\left\|\boldsymbol{\phi}(\boldsymbol{u}_1, t) - \boldsymbol{\phi}(\boldsymbol{u}_2, t)\right\|_2 \left\|\boldsymbol{f}(\boldsymbol{\Phi}_t(u_1)) - \boldsymbol{f}(\boldsymbol{\Phi}_t(u_2))\right\|_2 \\
&\le t\left\|\boldsymbol{\phi}(\boldsymbol{u}_1, t) - \boldsymbol{\phi}(\boldsymbol{u}_2, t)\right\|_2 L_f \left\|\boldsymbol{\Phi}_t(u_1) - \boldsymbol{\Phi}_t(u_2)\right\|_2.
\end{aligned}$$

Therefore,

$$\begin{aligned}
\frac{d}{dt}\Big(t\left\|\boldsymbol{\phi}(\boldsymbol{u}_1, t) - \boldsymbol{\phi}(\boldsymbol{u}_2, t)\right\|_2\Big) &\le L_f\left\|\boldsymbol{\Phi}_t(u_1) - \boldsymbol{\Phi}_t(u_2)\right\|_2 \\
&= L_f\left\|\boldsymbol{u}_1 + t\boldsymbol{\phi}(\boldsymbol{u}_1, t) - \boldsymbol{u}_2 - t\boldsymbol{\phi}(\boldsymbol{u}_2, t)\right\|_2 \\
&\le L_f\|\boldsymbol{u}_1 - \boldsymbol{u}_2\| + L_f t\left\|\boldsymbol{\phi}(\boldsymbol{u}_1, t) - \boldsymbol{\phi}(\boldsymbol{u}_2, t)\right\|_2 \qquad \forall t \in [0, T].
\end{aligned}$$

Applying the Gronwall inequality yields

$$t\left\|\boldsymbol{\phi}(\boldsymbol{u}_1, t) - \boldsymbol{\phi}(\boldsymbol{u}_2, t)\right\|_2 \le \Big(\mathrm{e}^{L_f t} - 1\Big)\left\|\boldsymbol{u}_1 - \boldsymbol{u}_2\right\|_2, \tag{21}$$

which gives (17) by taking $t = \Delta$ and then dividing it by Δ. The proof is completed. $\square$

We are now in a position to derive an error bound for the prediction model (16). Since it is well known that neural networks are universal approximator for a general class of functions, we will assume that the error of the approximation (9) is bounded and small.

Theorem 1. *Suppose $\boldsymbol{f}$ is Lipschitz continuous with Lipschitz constant L_f on a set $D \subseteq R^n$. Assume that $\boldsymbol{u}^{pre}(t_j) \in D_{\Delta_j}$ and $\boldsymbol{u}(t_j) \in D_{\Delta_j}$ for all $0 \le j < m$, and suppose that the generalization error of the approximation (9) for the trained neural network model is bounded, namely,*

$$\left\|\mathcal{N}_{\boldsymbol{\theta}} - \boldsymbol{\phi}\right\|_{L^\infty(D \times [\Delta_{\min}, \Delta_{\max}])} < +\infty,$$

where $\Delta_{\min} = \min_j \Delta_j$ and $\Delta_{\max} = \max_j \Delta_j$. Then we have

$$\left\|\boldsymbol{u}^{pre}(t_j) - \boldsymbol{u}(t_j)\right\|_2 \le \left\|\mathcal{N}_{\boldsymbol{\theta}} - \boldsymbol{\phi}\right\|_{L^\infty(D \times [\Delta_{\min}, \Delta_{\max}])} \sum_{s=1}^{j} \Delta_s \mathrm{e}^{L_f(t_j - t_s)} \qquad j = 1, \ldots, m.$$

In particular, if $\Delta_j \equiv \Delta$ for all $0 \le j < m$, then we have

$$\left\|\boldsymbol{u}^{pre}(t_j) - \boldsymbol{u}(t_j)\right\|_2 \le \left\|\mathcal{N}_{\boldsymbol{\theta}} - \boldsymbol{\phi}\right\|_{L^\infty(D \times [\Delta_{\min}, \Delta_{\max}])} \frac{\Delta(1 - \mathrm{e}^{L_f j\Delta})}{1 - \mathrm{e}^{L_f \Delta}}.$$

Proof. Let $\mathcal{E}_j = \|\boldsymbol{u}^{pre}(t_j) - \boldsymbol{u}(t_j)\|_2$, $j = 0, 1, \ldots, m$, denote the prediction errors. Note that

$$\boldsymbol{u}(t_{j+1}) = \boldsymbol{u}(t_j) + \Delta_j \boldsymbol{\phi}(\boldsymbol{u}(t_j), \Delta_j).$$

This together with the second equation in (16) yields

$$
\begin{aligned}
\mathcal{E}_{j+1} &= \left\|\boldsymbol{u}^{pre}(t_{j+1}) - \boldsymbol{u}(t_{j+1})\right\|_2 \\
&= \left\|\boldsymbol{u}^{pre}(t_j) + \Delta_j \mathcal{N}_\theta(\boldsymbol{u}^{pre}(t_j), \Delta_j) - \boldsymbol{u}(t_j) - \Delta_j \boldsymbol{\phi}(\boldsymbol{u}(t_j), \Delta_j)\right\|_2 \\
&\le \left\|\boldsymbol{u}^{pre}(t_j) - \boldsymbol{u}(t_j)\right\|_2 + \Delta_j \left\|\mathcal{N}_\theta(\boldsymbol{u}^{pre}(t_j), \Delta_j) - \boldsymbol{\phi}(\boldsymbol{u}(t_j), \Delta_j)\right\|_2 \\
&\le \mathcal{E}_j + \Delta_j \left(\left\|\mathcal{N}_\theta(\boldsymbol{u}^{pre}(t_j), \Delta_j) - \boldsymbol{\phi}(\boldsymbol{u}^{pre}(t_j), \Delta_j)\right\|_2 + \left\|\boldsymbol{\phi}(\boldsymbol{u}^{pre}(t_j), \Delta_j) - \boldsymbol{\phi}(\boldsymbol{u}(t_j), \Delta_j)\right\|_2\right),
\end{aligned}
$$

where we have used the triangle inequalities. Using Lemma 1 gives

$$\mathcal{E}_{j+1} \le \mathcal{E}_j + \Delta_j \left(\left\|\mathcal{N}_\theta(\boldsymbol{u}^{pre}(t_j), \Delta_j) - \boldsymbol{\phi}(\boldsymbol{u}^{pre}(t_j), \Delta_j)\right\|_2 + \frac{\mathrm{e}^{L_f \Delta_j} - 1}{\Delta_j}\left\|\boldsymbol{u}^{pre}(t_j) - \boldsymbol{u}(t_j)\right\|_2\right) \tag{22}$$

$$= \mathrm{e}^{L_f \Delta_j}\mathcal{E}_j + \Delta_j\left\|\mathcal{N}_\theta(\boldsymbol{u}^{pre}(t_j), \Delta_j) - \boldsymbol{\phi}(\boldsymbol{u}^{pre}(t_j), \Delta_j)\right\|_2 \tag{23}$$

$$\le \mathrm{e}^{L_f \Delta_j}\mathcal{E}_j + \Delta_j\left\|\mathcal{N}_\theta - \boldsymbol{\phi}\right\|_{L^\infty(D\times[\Delta_{\min}, \Delta_{\max}])}. \tag{24}$$

It follows that

$$
\begin{aligned}
\mathrm{e}^{-L_f t_{j+1}}\mathcal{E}_{j+1} &\le \mathrm{e}^{-L_f t_j}\mathcal{E}_j + \Delta_j \mathrm{e}^{-L_f t_{j+1}}\left\|\mathcal{N}_\theta - \boldsymbol{\phi}\right\|_{L^\infty(D\times[\Delta_{\min}, \Delta_{\max}])} \\
&\le \mathrm{e}^{-L_f t_{j-1}}\mathcal{E}_{j-1} + \left(\Delta_j \mathrm{e}^{-L_f t_{j+1}} + \Delta_{j-1}\mathrm{e}^{-L_f t_j}\right)\left\|\mathcal{N}_\theta - \boldsymbol{\phi}\right\|_{L^\infty(D\times[\Delta_{\min}, \Delta_{\max}])} \\
&\le \cdots \\
&\le \mathrm{e}^{-L_f t_0}\mathcal{E}_0 + \left(\Delta_j \mathrm{e}^{-L_f t_{j+1}} + \Delta_{j-1}\mathrm{e}^{-L_f t_j} + \cdots + \Delta_0 \mathrm{e}^{-L_f t_1}\right)\left\|\mathcal{N}_\theta - \boldsymbol{\phi}\right\|_{L^\infty(D\times[\Delta_{\min}, \Delta_{\max}])} \\
&= \left\|\mathcal{N}_\theta - \boldsymbol{\phi}\right\|_{L^\infty(D\times[\Delta_{\min}, \Delta_{\max}])}\sum_{s=0}^{j}\Delta_s \mathrm{e}^{-L_f t_{s+1}},
\end{aligned}
$$

where $\mathcal{E}_0 = 0$ has been used. Therefore, we have

$$\mathcal{E}_{j+1} \le \left\|\mathcal{N}_\theta - \boldsymbol{\phi}\right\|_{L^\infty(D\times[\Delta_{\min}, \Delta_{\max}])}\sum_{s=0}^{j}\Delta_s \mathrm{e}^{L_f(t_{j+1}-t_{s+1})} = \left\|\mathcal{N}_\theta - \boldsymbol{\phi}\right\|_{L^\infty(D\times[\Delta_{\min}, \Delta_{\max}])}\sum_{s=1}^{j+1}\Delta_s \mathrm{e}^{L_f(t_{j+1}-t_s)}.$$

If $\Delta_j \equiv \Delta$ for all j, then

$$\sum_{s=1}^{j}\Delta_s \mathrm{e}^{L_f(t_j - t_s)} = \Delta\sum_{s=1}^{j}\mathrm{e}^{L_f(j-s)\Delta} = \frac{\Delta(1 - \mathrm{e}^{L_f j\Delta})}{1 - \mathrm{e}^{L_f \Delta}}.$$

The proof is completed. $\qquad\square$

3.4. Robustness and variance of prediction

Let $\Delta_1 + \Delta_2 = T$ and $\Delta_1' + \Delta_2' = T$ represent two partitions of the interval $[0, T]$. By incorporating the semigroup property (12) into the learning process, the trained OSG-Net model satisfies

$$\mathbf{N}_\theta\left(\mathbf{N}_\theta\left(\boldsymbol{u}_0, \Delta_1\right), \Delta_2\right) \approx \mathbf{N}_\theta\left(\boldsymbol{u}_0, T\right) \approx \mathbf{N}_\theta\left(\mathbf{N}_\theta\left(\boldsymbol{u}_0, \Delta_1'\right), \Delta_2'\right),$$

which implies that

$$\left\|\mathbf{N}_\theta\left(\mathbf{N}_\theta\left(\boldsymbol{u}_0, \Delta_1\right), \Delta_2\right) - \mathbf{N}_\theta\left(\mathbf{N}_\theta\left(\boldsymbol{u}_0, \Delta_1'\right), \Delta_2'\right)\right\|_2$$

is small. In general, let

$$\left\{\Delta_j^{(k)} > 0 : \Delta_0^{(k)} + \Delta_1^{(k)} + \ldots + \Delta_n^{(k)} = T\right\}, \qquad k = 1, \ldots, K$$

11

denote K different partitions of $[0, T]$. It is expected that

$$\left\| \mathbf{N}_\theta \left(\cdots \mathbf{N}_\theta \left(\mathbf{N}_\theta \left(\boldsymbol{u}_0, \Delta_0^{(k)} \right), \Delta_1^{(k)} \right) \cdots \Delta_n^{(k)} \right) - \mathbf{N}_\theta \left(\cdots \mathbf{N}_\theta \left(\mathbf{N}_\theta \left(\boldsymbol{u}_0, \Delta_0^{(s)} \right), \Delta_1^{(s)} \right) \cdots \Delta_n^{(s)} \right) \right\|_2 \le \epsilon \quad \forall k, s \in \{1, \ldots, K\} \quad (25)$$

for some small number $\epsilon > 0$, which means the prediction results of the OSG-Net model are not sensitive to the time partition steps. Define

$$\begin{cases} \boldsymbol{u}_k^{pre}(0) = \boldsymbol{u}_0 \\ \boldsymbol{u}_k^{pre}(t_{j+1}^{(k)}) = \mathbf{N}_\theta(\boldsymbol{u}_k^{pre}(t_j^{(k)}), \Delta_j^{(k)}), \qquad j = 0, 1, \ldots, n \end{cases} \quad (26)$$

as the predicted states through different partitions, where $t_{j+1}^{(k)} = t_j^{(k)} + \Delta_j^{(k)}$ with $t_0^{(k)} = 0$ and $t_{n+1}^{(k)} = T$ for all $1 \le k \le K$.

Theorem 2. *Let $\mathcal{E}_T^{(k)} := \left\| \boldsymbol{u}_k^{pre}(T) - u(T) \right\|_2$ be the prediction error by the trained OSG-Net model via the kth temporal partition, where $u(T)$ denotes the true solution at time $t = T$. Under the assumption (25), we have the following estimate for the standard deviation of the prediction errors:*

$$\sqrt{\frac{1}{K} \sum_{k=1}^{K} \left(\mathcal{E}_T^{(k)} - \frac{1}{K} \sum_{s=1}^{K} \mathcal{E}_T^{(s)} \right)^2} \le \left(\frac{K-1}{K} \right) \epsilon. \quad (27)$$

Proof. Based on (25), we have

$$\left\| \boldsymbol{u}_k^{pre}(T) - \boldsymbol{u}_s^{pre}(T) \right\| \le \epsilon \qquad \forall k, s \in \{1, \ldots, K\}.$$

The triangle inequality implies that

$$\mathcal{E}_T^{(k)} := \left\| \boldsymbol{u}_k^{pre}(T) - u(T) \right\|_2 \le \left\| \boldsymbol{u}_s^{pre}(T) - u(T) \right\|_2 + \left\| \boldsymbol{u}_k^{pre}(T) - \boldsymbol{u}_s^{pre}(T) \right\|_2 = \mathcal{E}_T^{(s)} + \epsilon \qquad \forall k, s \in \{1, \ldots, K\}.$$

It follows that

$$(K-1)\mathcal{E}_T^{(k)} \le \sum_{s \ne k} \left(\mathcal{E}_T^{(s)} + \epsilon \right) = (K-1)\epsilon + \sum_{s=1}^{K} \mathcal{E}_T^{(s)} - \mathcal{E}_T^{(k)}.$$

Thus we have

$$\mathcal{E}_T^{(k)} \le \frac{K-1}{K} \epsilon + \frac{1}{K} \sum_{s=1}^{K} \mathcal{E}_T^{(s)}, \qquad 1 \le k \le K. \quad (28)$$

Similar, one can derive that

$$\mathcal{E}_T^{(k)} := \left\| \boldsymbol{u}_k^{pre}(T) - u(T) \right\|_2 \ge \left\| \boldsymbol{u}_s^{pre}(T) - u(T) \right\|_2 - \left\| \boldsymbol{u}_k^{pre}(T) - \boldsymbol{u}_s^{pre}(T) \right\|_2 = \mathcal{E}_T^{(s)} - \epsilon \qquad \forall k, s \in \{1, \ldots, K\}.$$

which yields

$$\mathcal{E}_T^{(k)} \ge -\frac{K-1}{K} \epsilon + \frac{1}{K} \sum_{s=1}^{K} \mathcal{E}_T^{(s)}, \qquad 1 \le k \le K. \quad (29)$$

Combining (28) with (29) gives

$$\left| \mathcal{E}_T^{(k)} - \frac{1}{K} \sum_{s=1}^{K} \mathcal{E}_T^{(s)} \right| \le \frac{K-1}{K} \epsilon \qquad \forall k \in \{1, \ldots, K\}.$$

Therefore, we obtain

$$\frac{1}{K} \sum_{k=1}^{K} \left(\mathcal{E}_T^{(k)} - \frac{1}{K} \sum_{s=1}^{K} \mathcal{E}_T^{(s)} \right)^2 \le \frac{1}{K} \sum_{k=1}^{K} \left(\frac{K-1}{K} \right)^2 \epsilon^2 = \left(\frac{K-1}{K} \right)^2 \epsilon^2,$$

which leads to (27). The proof is completed. $\square$

Remark 6 (Robustness and long-time stability). Theorem 2 shows the variance of the prediction errors via different partitions is small, indicating that the predicted results of the OSG-Net model are well self-matched and consistent for different time stepsizes. This property is highly desirable for robust prediction. A conventional model without embedding the semigroup structure may deviate from this property due to the error accumulation at each forward step and thus suffers from poor performance in long-time prediction, as the error often grows in an exponential manner when the model is recursively composed. Our numerical experiments in Section 5 will further demonstrate our OSG-Net model (especially the main GDSG approach) is very stable in long-time prediction and is much more robust than the baseline approach; see, for example, Figures 5 and 20.

Remark 7. The predictive OSG-Net model (16) resembles an explicit algorithm for evolution prediction. However, the time stepsize of our model can be set very large and would not suffer from a standard time step restriction, which is typically required by traditional explicit numerical schemes. This is true even for some highly stiff problems (see the examples in Section 5).

4. Extension of Deep-OSG approach to modeling unknown PDEs

Motivated by the previous work [30, 31], our Deep-OSG framework can be easily extended to data-driven modeling of unknown PDEs. Consider an unknown time-dependent PDE:

$$\begin{cases} \partial_t u = \mathcal{L}(u), & (x, t) \in \Omega \times \mathbb{R}^+, \\ \mathcal{B}(u) = 0, & (x, t) \in \partial\Omega \times \mathbb{R}^+, \\ u(x, 0) = u_0(x), & x \in \bar{\Omega}, \end{cases} \tag{30}$$

where $\Omega \subseteq \mathbb{R}^d$ is the physical domain, and $\mathcal{L}$ and $\mathcal{B}$ respectively represent the operators in the equations and boundary conditions. We assume that the operator $\mathcal{L}$ is unknown, and we focus on learning PDE in the interior of the domain with given boundary conditions.

As our attention is restricted to autonomous PDEs, the unknown governing equations admit an evolution operator

$$\mathbf{\Phi}_\Delta : \mathbb{V} \to \mathbb{V}, \qquad \mathbf{\Phi}_\Delta u(\cdot, t) = u(\cdot, t + \Delta),$$

where $\mathbb{V}$ is assumed to be an infinite-dimensional Hilbert space. Note that only the time difference Δ is relevant for the evolution operator of autonomous systems, as the time variable t can be shifted arbitrarily. Assume that the solution $u(x, t)$ is measurable or observable, namely, the snapshots of u are available at certain time instances:

$$u(x, t_k^{(i)}), \qquad k = 1, \ldots, K_i, \qquad i = 1, \cdots, I_{traj}, \tag{31}$$

where i denotes the i-th "trajectory" along which K_i snapshot data are collected. Our goal is to learn the evolution operator of the underlying PDE based on the snapshot data.

Unlike ODEs, for PDEs the exact evolution operator is defined on an infinite-dimensional space. To make the PDE learning problem tractable, we should first reduce the problem into finite dimensions in either nodal or modal spaces [30, 31]; see Figure 3 for illustration.

4.1. Learning PDEs via Deep-OSG approach in nodal space

Assume that the data (31) are sampled on a set of spatial nodal points or grids

$$\mathbb{X}_N = \{x_1, \ldots, x_N\} \subset \Omega.$$

Define

$$\mathbf{U}_k^i = \left(u(x_1, t_k^{(i)}), \ldots, u(x_N, t_k^{(i)})\right)^\top, \qquad k = 1, \ldots, K_i, \qquad i = 1, \cdots, I_{traj}. \tag{32}$$

Define

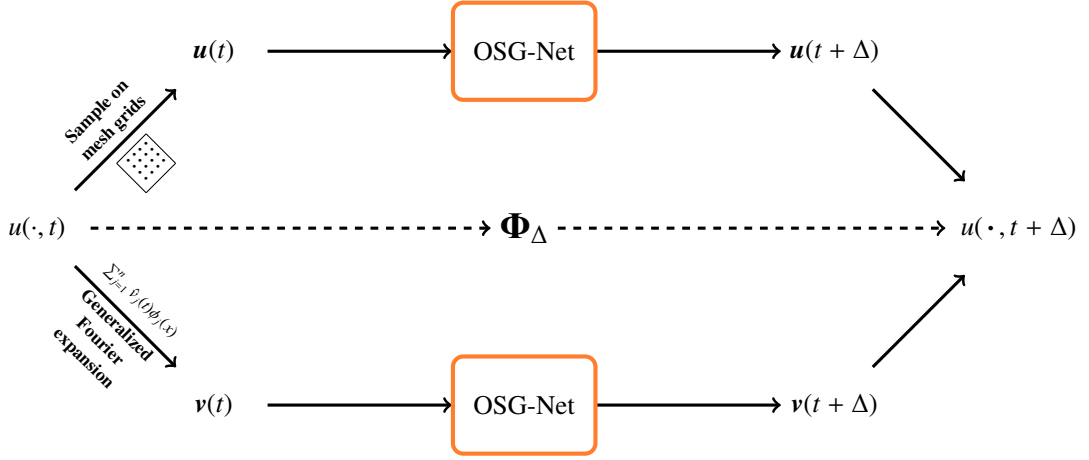$$\mathbf{U}(t) = (u(x_1, t), \ldots, u(x_N, t))^\top.$$

13

Fig. 3: **Learning PDE evolution operator in nodal and modal spaces**.

In order to approximate the (unknown) infinite-dimensional evolution operator $\mathbf{\Phi}_\Delta$ in the nodal space, we consider a finite-dimensional evolution operator $\widehat{\mathbf{\Phi}}_\Delta$, which evolves $\mathbf{U} \in \mathbb{R}^N$, namely,

$$\widehat{\mathbf{\Phi}}_\Delta : \mathbb{R}^N \to \mathbb{R}^N, \qquad \widehat{\mathbf{\Phi}}_\Delta \mathbf{U}(t) = \mathbf{U}(t + \Delta). \tag{33}$$

This operator closely resembles the evolution operators of spectral collocation methods and finite difference methods for solving a known PDE. Note that here we assume that an autonomous PDE can be effectively approximated by an autonomous discrete system via proper spatial approximation as in a semi-discrete numerical scheme for a known PDE.

Now our goal becomes to approximate $\widehat{\mathbf{\Phi}}_\Delta$ using the data (32). As the ODE case, we regroup the data (32) in the following form

$$\left\{ \boldsymbol{U}_{0,j}, \ \Delta_{1,j}, \ \boldsymbol{U}_{1,j}, \ \Delta_{2,j}, \ \boldsymbol{U}_{3,j} \right\}_{j=1}^{J} \tag{34}$$

with $J = \sum_{i=1}^{I_{traj}} (K_i - 2)$. Then we use this dataset to train an OSG-Net $\mathbf{N}_\theta$ for learning the finite-dimensional evolution operator $\widehat{\mathbf{\Phi}}_\Delta$, namely, $\mathbf{N}_\theta \approx \widehat{\mathbf{\Phi}}_\Delta$.

Once the OSG-Net $\mathbf{N}_\theta$ is successfully trained, we can use it to conduct prediction of the unknown PDE system on the nodal grids. For an arbitrary initial condition $u_0(x) \in \mathbb{V}$, we recursively apply the trained OSG-Net $\mathbf{N}_\theta$ to obtain

$$\begin{cases} \mathbf{U}^{pre}(t_0) = (u_0(x_1), \ldots, u_0(x_N))^\top, \\ \boldsymbol{U}^{pre}(t_{j+1}) = \mathbf{N}_\theta(\boldsymbol{U}^{pre}(t_j), \Delta_j), \qquad j = 0, 1, \ldots \end{cases} \tag{35}$$

with $\Delta_j = t_{j+1} - t_j$. The function approximation to $u(x, t_j)$ can be obtained by using some interpolation, fitting, or reconstruction techniques.

Since the proposed OSG-Net architecture and the semigroup-informed loss function are non-intrusive to the basic network structures, the Deep-OSG framework is very feasible. Besides FNN, the OSG-Net architecture can also be combined with other suitable basic networks, such as the special neural network designed in [31] for learning PDEs in nodal space, the convolution neural networks, the Fourier neural operators (FNO) [43], and the locally connected networks, etc.

4.2. Learning PDEs via Deep-OSG approach in modal space

The proposed Deep-OSG approach can also be generalized to learn evolution operator in modal space, i.e. the generalized Fourier space. Let $\mathbb{V}_n$ denote a finite-dimensional subspace of $\mathbb{V}$. We first select a set of basis functions of $\mathbb{V}_n$:

$$\{\phi_1(x), ..., \phi_n(x)\}.$$

define on the physical domain Ω. The solution of the underlying PDE can be approximated in $\mathbb{V}_n$ by a finite-term series as

$$u(x,t) \approx \sum_{j=1}^{n} v_j(t)\phi_j(x) =: u_n(x,t),$$

where $\{v_j\}_{j=1}^{n}$ are the modal expansion coefficients. Such an approximation may be given by a projection of $u(x,t)$ onto the finite-dimensional subspace $\mathbb{V}_n$. Let $\mathcal{P}_n : \mathbb{V} \to \mathbb{V}_n$ denote the projection operator. Define the vectors

$$\mathbf{V}(t) := (v_1(t), \ldots, v_n(t))^{\top}, \quad \mathbf{\Phi}(x) = (\phi_1(x), ..., \phi_n(x))^{\top}.$$

We introduce the following linear mapping

$$\Pi : \mathbb{R}^n \to \mathbb{V}_n, \qquad \Pi\mathbf{V} = \langle \mathbf{V}, \mathbf{\Phi}(x) \rangle,$$

which defines a unique correspondence between a solution in $\mathbb{V}_n$ and its modal expansion coefficients vector in $\mathbb{R}^n$, because Π is a bijective mapping.

In order to approximate the (unknown) infinite-dimensional evolution operator $\mathbf{\Phi}_\Delta$ in the modal space, we consider a finite-dimensional evolution operator $\widetilde{\mathbf{\Phi}}_\Delta$, which evolves the modal expansion coefficients vector $\mathbf{V}(t) \in \mathbb{R}^n$, namely,

$$\widetilde{\mathbf{\Phi}}_\Delta : \mathbb{R}^n \to \mathbb{R}^n, \qquad \widetilde{\mathbf{\Phi}}_\Delta \mathbf{V}(t) = \mathbf{V}(t + \Delta). \tag{36}$$

Mathematically, this evolution operator can be expressed as

$$\widetilde{\mathbf{\Phi}}_\Delta = \Pi^{-1} \mathcal{P}_n \mathbf{\Phi}_\Delta \Pi.$$

This operator closely resembles the evolution operators of spectral Galerkin methods for solving a known PDE. Again, we assume that an autonomous PDE can be effectively approximated by an autonomous discrete system via proper spatial approximation as in a semi-discrete numerical scheme for a known PDE.

Now our goal is transferred to learn the finite-dimensional operator $\widetilde{\mathbf{\Phi}}_\Delta$ for modal expansion coefficients. Given the snapshot data (31), we first project them onto the finite-dimensional subspace $\mathbb{V}_n$ and compute the modal expansion coefficients:

$$\mathbf{V}_k^i = \Pi^{-1} \mathcal{P}_n u(x, t_k^{(i)}), \qquad k = 1, \ldots, K_i, \qquad i = 1, \cdots, I_{traj}. \tag{37}$$

We then follow the ODE case and regroup the data (37) in the following form

$$\left\{ \mathbf{V}_{0,j}, \ \Delta_{1,j}, \ \mathbf{V}_{1,j}, \ \Delta_{2,j}, \ \mathbf{V}_{3,j} \right\}_{j=1}^{J} \tag{38}$$

with $J = \sum_{i=1}^{I_{traj}} (K_i - 2)$. We employ this dataset (38) to train an OSG-Net $\mathbf{N}_\theta$ for learning the finite-dimensional evolution operator $\widetilde{\mathbf{\Phi}}_\Delta$, namely, $\mathbf{N}_\theta \approx \widetilde{\mathbf{\Phi}}_\Delta$.

Once the OSG-Net $\mathbf{N}_\theta$ is successfully trained, we can use it to conduct prediction of the unknown PDE system. For an arbitrary initial condition $u_0(x) \in \mathbb{V}$, we recursively apply the trained OSG-Net $\mathbf{N}_\theta$ to obtain

$$\begin{cases} \mathbf{V}^{pre}(t_0) = \Pi^{-1} \mathcal{P}_n u_0(x), \\ \mathbf{V}^{pre}(t_{j+1}) = \mathbf{N}_\theta(\mathbf{V}^{pre}(t_j), \Delta_j), \qquad j = 0, 1, \ldots \end{cases} \tag{39}$$

with $\Delta_j = t_{j+1} - t_j$. The predicted solution $u^{pre}(x, t_j)$ is then obtained by

$$u^{pre}(x, t_j) = \Pi\mathbf{V}^{pre}(t_j) = \langle \mathbf{V}^{pre}(t_j), \mathbf{\Phi}(x) \rangle = \sum_{i=1}^{n} v_i^{pre}(t_j)\phi_i(x)$$

with $(v_1^{pre}, \ldots, v_n^{pre})^{\top} = \mathbf{V}^{pre}$.

5. Numerical experiments

In this section, we conduct several numerical experiments to demonstrate the effectiveness and robustness of the proposed Deep-OSG approach. The studied cases cover a wide range of ODEs and PDEs. For benchmarking purpose, the true governing equations are given in all the examples, but we only use the true equations to generate training, validation, and test data. All the data are generated by using either analytical solutions or high-order accurate numerical methods of the true equations. The dataset is organized into a number of bursts with two forward steps as in (6). Instead of generating a sufficiently large dataset as in [29, 30, 31], we will only use a relatively small dataset for training, so as to mimic the practical situations that the measurement data are very limited due to resource constraints or experimental accessibility. In practice, the measurement data may be often collected with varied time steps. Thus, in our setup, we randomly sample the time stepsize from a pre-defined interval $[\Delta_{\min}, \Delta_{\max}]$. Before training we normalize the data to $[-1, 1]$ for a better performance (see Appendix A.1 for a comparison between normalized and non-normalized datasets) [1]. When training the neural networks, 10% of data are used for validation, and the updated model is saved after each mini-batch only when the validation loss decreases. Throughout this section, we employ the Gaussian Error Linear Unit (GELU) activation for the hidden neurons in OSG-Nets. The Adam algorithm with a cyclic learning rate scheduler [47] is employed for training. All our neural network models are trained by using the open-source Tensorflow library [48].

Remark 8 (Dynamic validation). When the dataset is very small (for example, there are only 10 bursts of trajectory data for learning linear ODEs in Section 5.1.1), the validation data (10% of whole data) would be too small to represent the model generalization error. To address this issue, we propose a dynamic dataset splitting technique for training and validation, *i.e.*, the entire dataset is shuffled after every epoch and then we dynamically split into a training set and a validation set. As a result, the dynamic validation dataset is a more reliable estimator to the generalization error, and the whole dataset is dynamically used for back-propagation. We observe a notable advantage of this technique when the entire dataset is small; see Appendix A.2 for a comparison.

Once a fully trained OSG-Net model is obtained, we will use it to conduct predictions of the solution and compare them against the reference solution produced by the true governing equations. Specifically, we evaluate the performance for long-time prediction based on the average relative l_2 error after the model marches forward many steps. This error is computed on a separate test dataset containing I long trajectories $\{u_i(t_0), u_i(t_1), ..., u_i(t_M)\}_{i=1}^{I}$ with $I = 100$ as follows:

$$\overline{\mathcal{E}} = \frac{1}{M} \sum_{m=1}^{M} \mathcal{E}(t_m) \quad \text{with} \quad \mathcal{E}(t_m) = \frac{1}{I} \sum_{i=1}^{I} \frac{\|u_i(t_m) - u_i^{pre}(t_m)\|_2}{\|u_i(t_m)\|_2}, \tag{40}$$

where each trajectory is generated by marching forward M times from the initial state $u_{k,0}$ with the time stepsize taken as $\Delta = (\Delta_{\min} + \Delta_{\max})/2$, and $u_i(t_m)$ and $u_i^{pre}(t_m)$ respectively denote the reference and predicted solutions at time $t_m = m\Delta$.

To examine the prediction robustness of the neural network models, we will also investigate the variance of prediction errors obtained through different partitions of the time interval $[0, T]$, where T is the final prediction time. We consider K random partitions with $K = 100$, and estimate the standard deviation of the prediction errors based on the I test trajectory data with $I = 100$ as follows:

$$\sigma = \frac{1}{I} \sum_{i=1}^{I} \sqrt{\frac{1}{K} \sum_{k=1}^{K} \left(\mathcal{E}_T^{k,i} - \frac{1}{K} \sum_{s=1}^{K} \mathcal{E}_T^{s,i} \right)^2} \quad \text{with} \quad \mathcal{E}_T^{k,i} := \frac{\|u_i(T) - u_{k,i}^{pre}(T)\|_2}{\|u_i(T)\|_2}, \ 1 \le k \le K, \ 1 \le i \le I, \tag{41}$$

where $u_{k,i}^{pre}(T)$ denotes the ith trajectory solution at time T predicted by the trained network model via the kth partition.

---

[1]The relative error on the test set is computed on the non-normalized data.

5.1. Numerical experiments on ODEs

5.1.1. ODE example 1: Linear ODEs

We first consider the following linear ODE system:

$$
\begin{cases}
\dfrac{du_1}{dt} = u_1 - 4u_2 + 3, \\[2mm]
\dfrac{du_2}{dt} = 4u_1 - 7u_2 + 3.
\end{cases}
\tag{42}
$$

The training data consist of only 10 bursts of short trajectories with two forward time steps $\{\Delta_{1,j}, \Delta_{2,j}\}_{j=1}^{10}$ randomly sampled from the interval $[0.05, 0.15]$ and the initial states of the trajectories randomly sampled from the domain $D = [0, 2] \times [0, 2]$. It is worth noting that the size of this dataset is much smaller than that used in [29], where more than ten thousands data pairs were employed for training. We adopt an OSG-Net with 3 fully-connected hidden layers, each of which has 30 neurons. This is an over-parameterization learning, as the number of the network parameters is much larger than the size of training dataset. The parameters in the loss of the GDSG method are set as $\lambda = 1$ and $Q = 5$. The network is trained for up to $100,000$ epochs with a batch size equal to 5.

Figure 4 shows the loss histories for the baseline, LISG, and GDSG methods. We see that the validation losses of the LISG and GDSG methods are larger than that of the baseline method. This is because the loss functions of the LISG and GDSG methods contain more terms.

However, the GDSG method reduces the semigroup loss much faster, reaching a level of 4–6 orders smaller than the baseline and LISG methods at the end of training. The semigroup loss of the baseline method almost does not decrease after the first $10,000$ epochs, while its validation loss is continuously reduced.
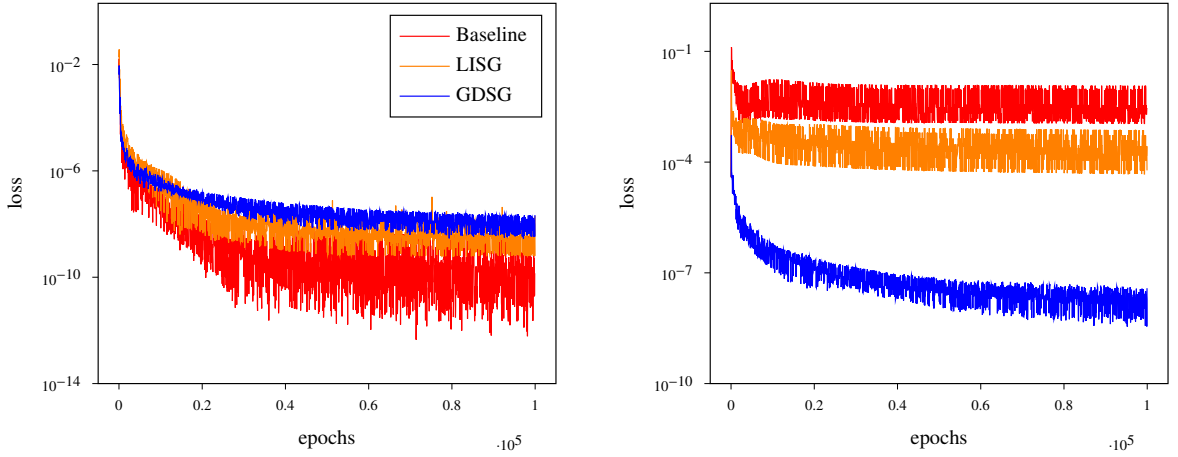
Fig. 4: Linear ODEs: Validation loss (left) and semi-group loss (right) during the training stage. The history is recorded every 50 epochs.

To validate the trained models, we employ 100 different initial conditions and march the trained models forward in time up to $t = 2$. The average relative l_2 errors $\{\mathcal{E}(t_m)\}_{m=1}^M$ defined by (40) with $M = 20$ are computed and shown in Figure 5. It is seen that the prediction errors of the GDSG method stay at a small level, the prediction errors of the LISG method increase slowly, while the prediction errors of the baseline method grow very fast. We choose a trajectory and show the predicted solutions as well as the portrait on the (u_1, u_2) phase plane. One can observe that the GDSG method produces the most accurate prediction. We also compute the standard deviation σ of the prediction errors defined in (41) for 100 different partitions of the time interval $[0, 2]$. The comparison is given in Table 1. The results show that the GDSG method is very robust and outperforms the baseline and LISG methods.

We now study the effects of the two parameters (λ, Q) in the loss function (13)–(14) of the GDSG method. The regularization factor λ weighs the importance of semigroup-informed loss over data-driven loss. As shown in Figure 7a, changing the value of λ has a notable impact on the prediction accuracy, and there exists an optimal value around 2 in the present case. For the second parameter Q, we observe positive effect when increasing Q until 5, after what
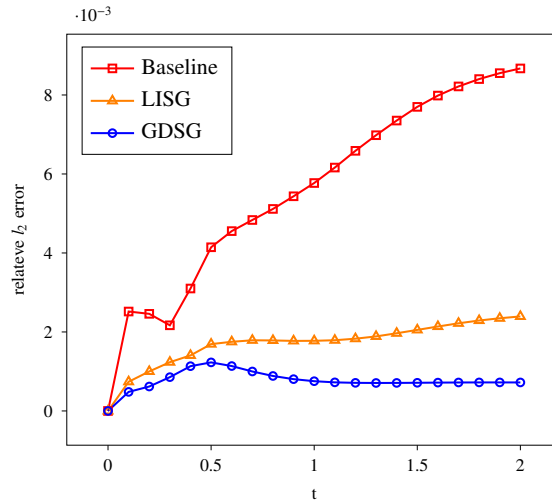
Fig. 5: Linear ODEs: Evolution of the prediction error over time.

Table 1: Linear ODEs: Comparisons of the average prediction error $\overline{\mathcal{E}}$ on the test set, the standard deviation σ of prediction errors, and the training time.

	Baseline	LISG	GDSG
Prediction error $\overline{\mathcal{E}}$	5.558×10^{-3}	1.708×10^{-3}	$\mathbf{7.652 \times 10^{-4}}$
Standard deviation σ	1.951×10^{-3}	3.440×10^{-4}	$\mathbf{4.932 \times 10^{-5}}$
Training time per epoch	$\mathbf{5.613 \times 10^{-3}}$	8.124×10^{-3}	8.909×10^{-3}

the benefit becomes negligible (see Figure 7b). It is worth noting that the loss function (13) with larger Q requires more storage and computational costs. Therefore, a moderate Q, e.g. $Q = 5$, is preferred. Table 1 gives a comparison of the CPU time (in seconds) of each training epoch[2] for the baseline, LISG, and GDSG methods.

We then consider the case of noisy data. The training data are set as

$$\left\{ \boldsymbol{u}_{0,j}(1 + \boldsymbol{\epsilon}_{0,j}), \Delta_{1,j}, \boldsymbol{u}_{1,j}(1 + \boldsymbol{\epsilon}_{1,j}), \Delta_{2,j}, \boldsymbol{u}_{2,j}(1 + \boldsymbol{\epsilon}_{2,j}) \right\}_{j=1}^{400},$$

where the relative noises $\boldsymbol{\epsilon}_{0,j}$, $\boldsymbol{\epsilon}_{1,j}$, and $\boldsymbol{\epsilon}_{2,j}$ are drawn from the uniform distribution over $[-\eta, \eta] \times [-\eta, \eta]$, with η standing for the noise level. We conduct two experiments with η set as 0.02 and 0.05, respectively. In Figure 8, we show the phase plots generated by the GDSG method. It can be seen that the main structure of the solution is still well captured by our method. Thanks to the use of integral form of the underlying equations in learning the evolution operator, our method tolerates the training noise quite well, as expected.

5.1.2. ODE example 2: Periodic attractor

This example considers a nonlinear ODE system with two variables:

$$\begin{cases} \dfrac{du_1}{dt} = u_2 - u_1(u_1^2 + u_2^2 - 1), \\ \dfrac{du_2}{dt} = -u_1 - u_2(u_1^2 + u_2^2 - 1) \end{cases} \tag{43}$$

---

[2]The training time is measured on the Intel® Core™ i9−12900K platform.
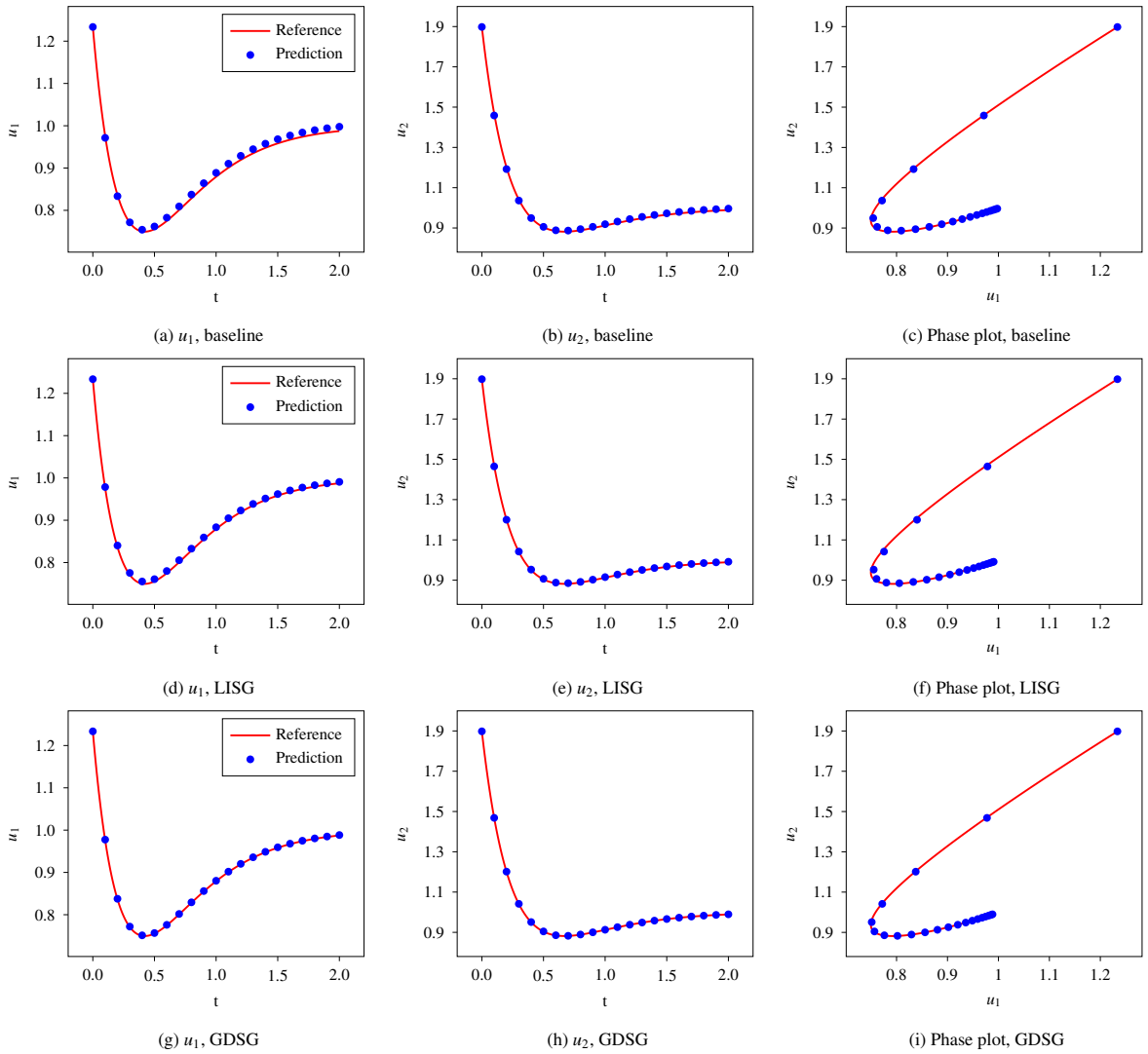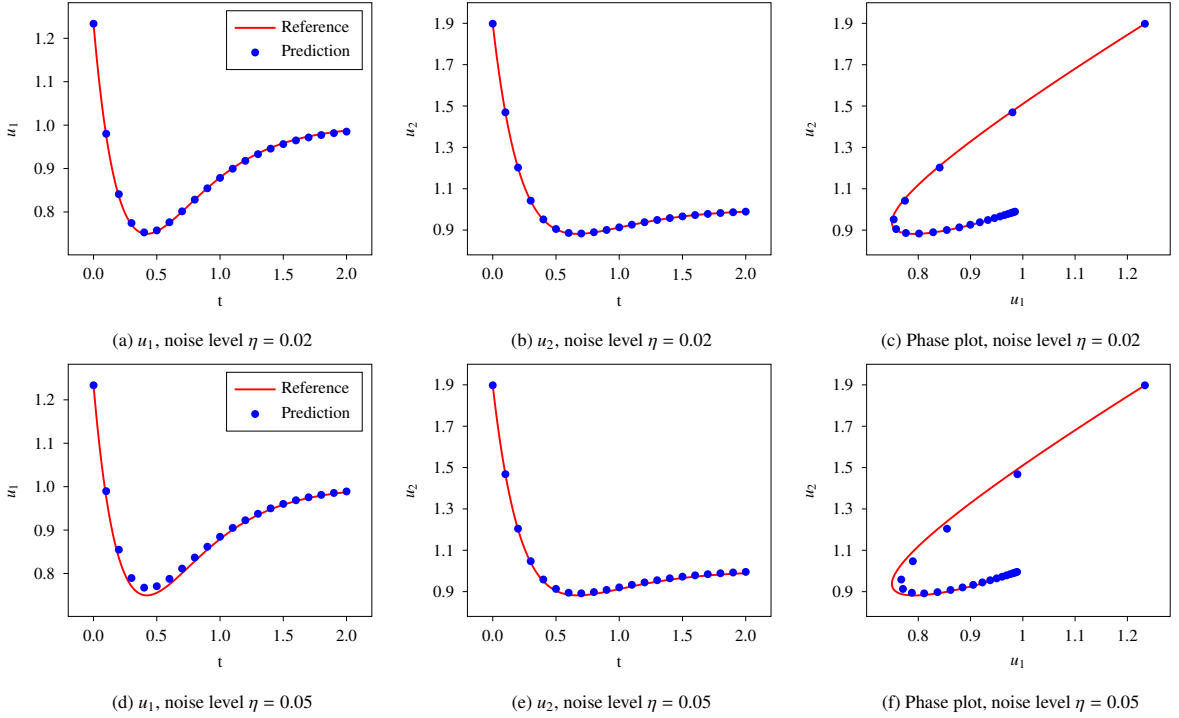
Fig. 6: Linear ODEs: Trajectory and phase plots with the initial state $(1.234, 1.898)$ for $t \in [0, 2]$. Top: baseline method. Middle: LISG method. Bottom: GDSG method with $\lambda = 1$ and $Q = 5$.

with the unit circle $\{(u_1, u_2) : u_1^2 + u_2^2 = 1\}$ being its periodic attractor. In this problem, the training data consist of 50 bursts of short trajectories with two forward time steps $\{\Delta_{1,j}, \Delta_{2,j}\}_{j=1}^{50}$ randomly sampled from the interval $[0.05, 0.15]$, and the initial states of the trajectories randomly sampled from the domain $D = [-2, 2] \times [-2, 2]$.

The two parameters in the loss function (13)–(14) of the GDSG method are set as $\lambda = 2$ and $Q = 5$. For neural network modeling, we adopt an OSG-Net with 3 fully-connected hidden layers, each of which has 60 neurons. The network is trained for up to $100,000$ epochs with a batch size of 5. Figure 9 presents the long-time prediction results of the GDSG method over time up to $t = 20$, *i.e.* forward steps $M = 200$. We see that the predicted trajectories agree well with the reference solution. The evolution of prediction error versus time is shown for the baseline, LISG, and GDSG methods in Figure 11, from which we observe slower error growth for the GDSG and LISG methods than the baseline method. This demonstrates the importance of embedding the semigroup property for the stability of long-time prediction.
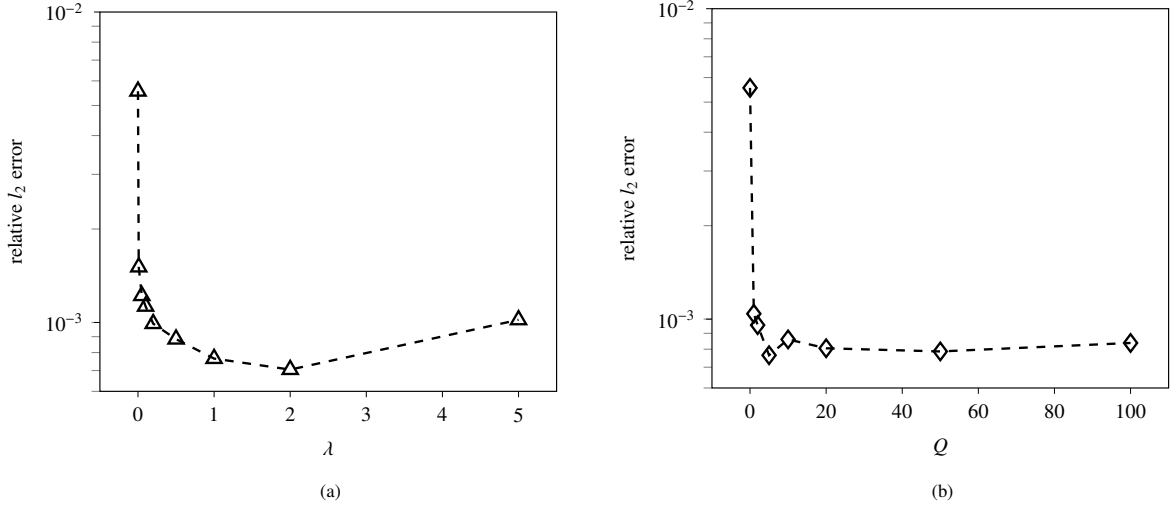
Fig. 7: Linear ODEs: Average prediction errors for the GDSG method with varied λ (left) and Q (right) in the loss function (13).

(a) u_1, noise level $\eta = 0.02$

(b) u_2, noise level $\eta = 0.02$

(c) Phase plot, noise level $\eta = 0.02$

(d) u_1, noise level $\eta = 0.05$

(e) u_2, noise level $\eta = 0.05$

(f) Phase plot, noise level $\eta = 0.05$

Fig. 8: Linear ODEs: Trajectory and phase plots with the initial state $(1.234, 1.898)$ for $t \in [0, 2]$. The prediction is obtained by the GDSG method with the training data containing 2% (top) and 5% noise, respectively.

5.1.3. ODE example 3: Damped pendulum

Now we consider the damped pendulum system [29], where the angle u_1 and velocity u_2 of the pendulum satisfy the following equations:

$$\begin{cases} \dfrac{du_1}{dt} = u_2, \\ \dfrac{du_2}{dt} = -\alpha u_2 - \beta \sin(u_1) \end{cases} \tag{44}$$

20

(a) u_1 and u_2, GDSG
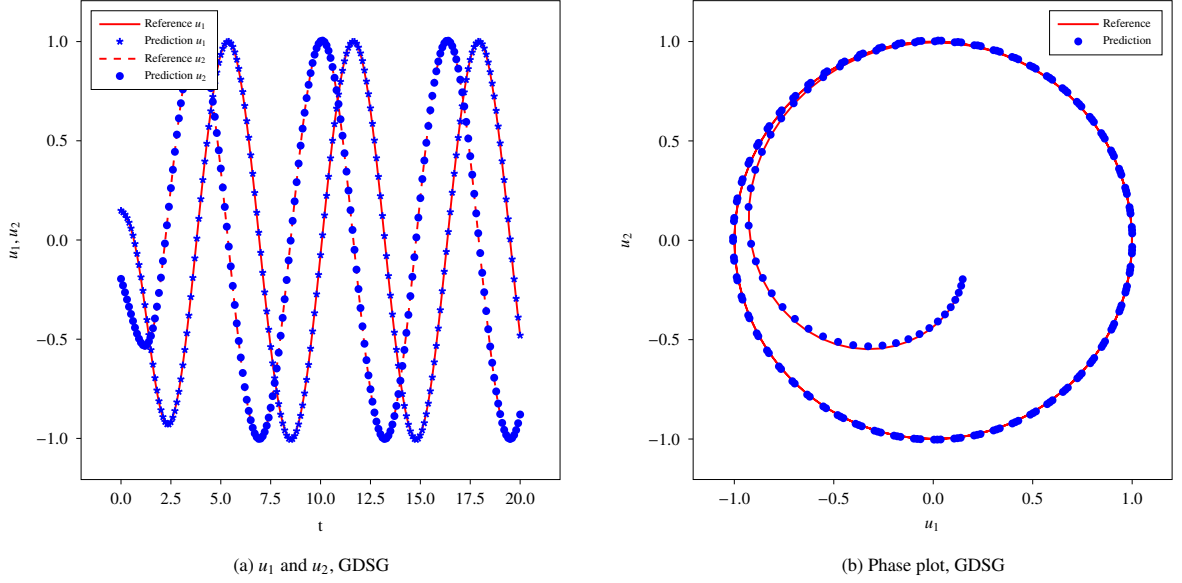
(b) Phase plot, GDSG

Fig. 9: Periodic attractor: Trajectory and phase plots with $\mathbf{u}_0 = (0.148, -0.196)$ for $t \in [0, 20]$. The prediction is obtained by the GDSG method.

with $\alpha = 0.2$ and $\beta = 9.8$. The training data consists of 100 bursts of short trajectories with two forward time steps $\{\Delta_{1,j}, \Delta_{2,j}\}_{j=1}^{50}$ randomly sampled from the interval $[0.05, 0.15]$, and the initial states of the trajectories randomly sampled from the domain $D = \left\{(u_1, u_2) : |u_1| \leq \pi, |u_2| \leq \min\left(2\pi, \sqrt{2\beta L(1 + \cos(u_1))}\right)\right\}$. Here $L = 1$ is the pendulum length, and the initial gravitational potential and kinetic energy $-\beta L \cos(u_1) + \frac{u_2^2}{2}$ is small enough to confine the pendulum in the domain $\{(u_1, u_2) : |u_1| \leq \pi\}$.

The two parameters of the GDSG method are set as $\lambda = 1$ and $Q = 5$. For neural network modeling, we adopt an OSG-Net with 3 fully-connected hidden layers, each of which has 60 neurons. The network is trained for up to $100,000$ epochs with a batch size of 5. Figure 10 presents the long-time prediction results of the GDSG method over time with $M = 200$ forward steps. The evolution of prediction error versus time is shown for the baseline, LISG, and GDSG methods in Figure 11. Similar to the periodic attractor problem, these results show again the importance of the embedded semigroup property for prediction stability and robustness.

(a) u_1 and u_2, GDSG
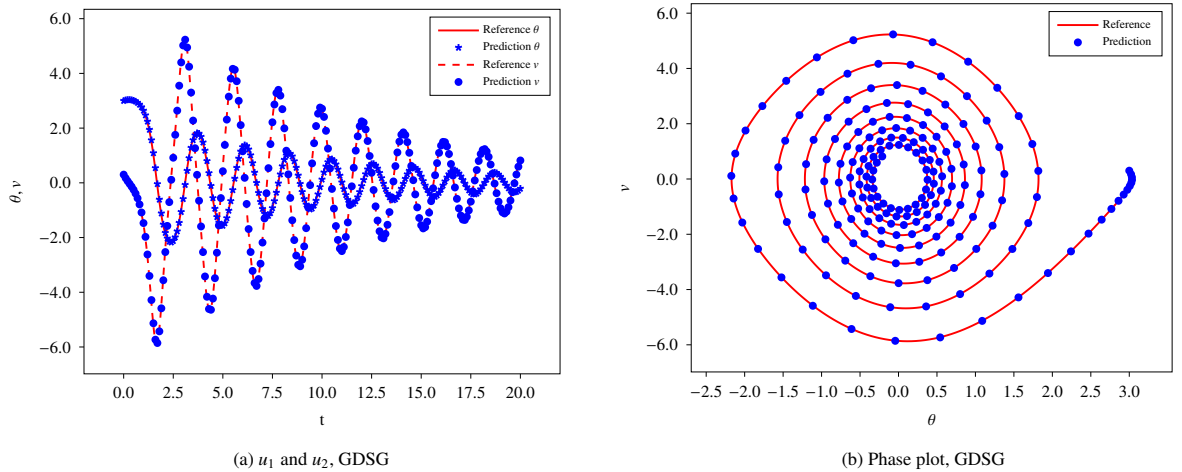
(b) Phase plot, GDSG

Fig. 10: Damped pendulum: Trajectory and phase plots with $\mathbf{u}_0 = (3.0, 0.3)$ for $t \in [0, 20]$. The prediction is obtained by the GDSG method.

21
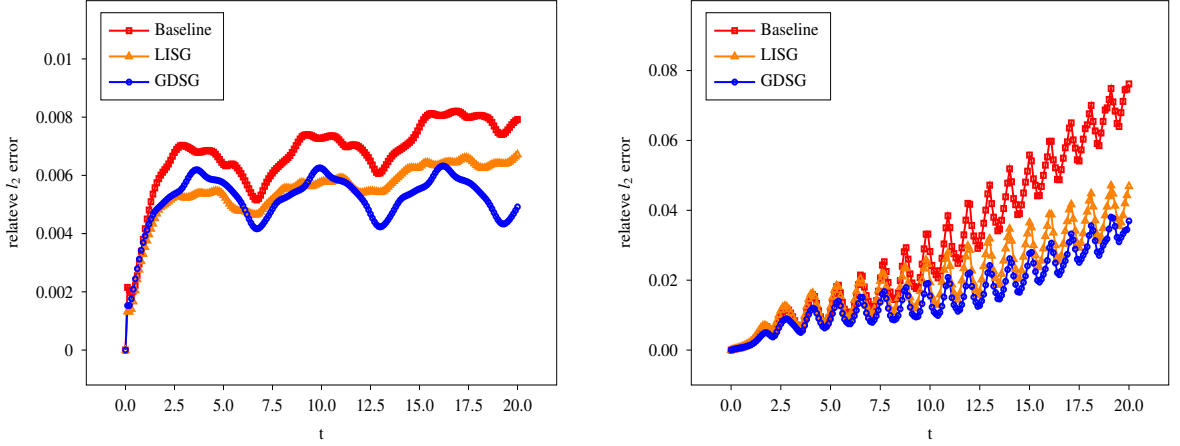
Fig. 11: Evolution of the average prediction error over time. Left: periodic attractor; Right: damped pendulum.

5.1.4. ODE example 4: Multiscale autocatalytic chemical reaction system

This is a challenging example concerning the kinetics of three chemical species, denoted by A, B, and C, respectively. The relevant dynamical system was proposed by Robertson [49] and is described by the following nonlinear stiff ODEs:

$$
\begin{cases}
\dfrac{du_1}{dt} = -k_1 u_1 + k_2 u_2 u_3, \\[2mm]
\dfrac{du_2}{dt} = k_1 u_1 - k_2 u_2 u_3 - k_3 u_2^2, \\[2mm]
\dfrac{du_3}{dt} = k_3 u_2^2,
\end{cases}
\tag{45}
$$

where (u_1, u_2, u_3) represent the concentrations of (A, B, C), with $u_1 + u_2 + u_3 = 1$. The reaction rates are $k_1 = 0.04$, $k_2 = 10^4$, and $k_3 = 3 \times 10^7$, making the system (45) very stiff. As shown in Figure 12, for the initial state $(1, 0, 0)$, the solution of this system goes through a rapid transition with the generation of catalyst B when $t \in [0, 10^{-3}]$, after what the reaction becomes smooth as A and B are transformed into C. To capture the dynamics at both small and large time scales, variable step model is highly desirable.

In order to demonstrate the capability of our methods in capturing such multiscale dynamics, we train different models based on two datasets.

- The first dataset consists of 500 bursts of trajectory data, which are used to train multiscale time-step models for learning the evolution operators from small to large time scales. For this purpose, we sample the time stepsizes from the interval $10^{U[-4.9, 0.1]}$, with $U[-4.9, 0.1]$ being the uniform distribution on $[-4.9, 0.1]$. To effectively capture the multiscale dynamics, the time-step input of the OSG-Net is modified to $-\log_{10}(\Delta)$, as described in Remark 2. We observe that such a modification is beneficial for efficiently reducing the training loss.

- The second dataset consists of 200 bursts of short trajectories with two forward time steps $\{\Delta_{1,j}, \Delta_{2,j}\}_{j=1}^{200}$ randomly sampled from a large interval $[5, 15]$ and the initial states of the trajectories randomly sampled from the domain $D = [0, 1] \times [0, 10^{-4}] \times [0, 1]$. The dataset is used to train large-scale models for predictions with large time steps.

For all the models, we use an OSG-Net with 3 fully-connected hidden layers, each of which has 60 neurons. The parameters in the loss function of the GDSG method are set as $\lambda = 1$ and $Q = 5$. The network is trained for up to $100,000$ epochs with a batch size of 5.
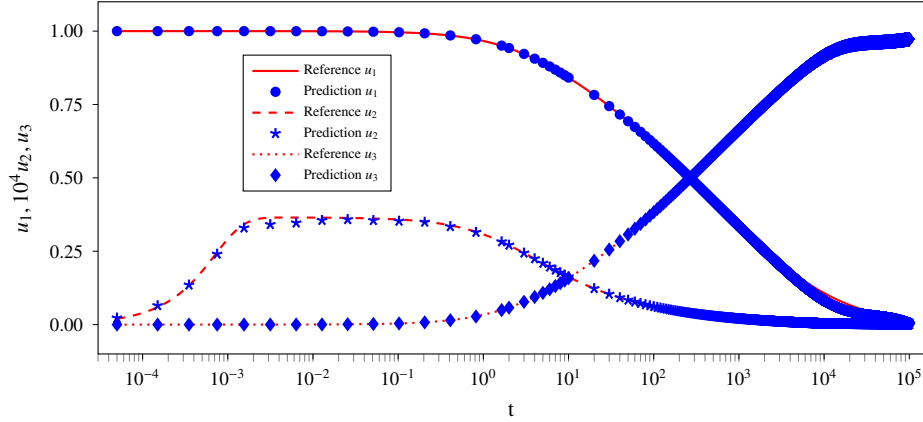
In Figure 12, we present the long-term prediction results by the trained models, starting from the initial condition $(1, 0, 0)$ and for time up to $t = 10^5$. In the first stage, the multi-scale model is used to predict the evolution from $t = 0$ to $t = 10$, with the time stepsize starting from $\Delta = 5 \times 10^{-5}$ and doubling after each forward step until it reaches

22
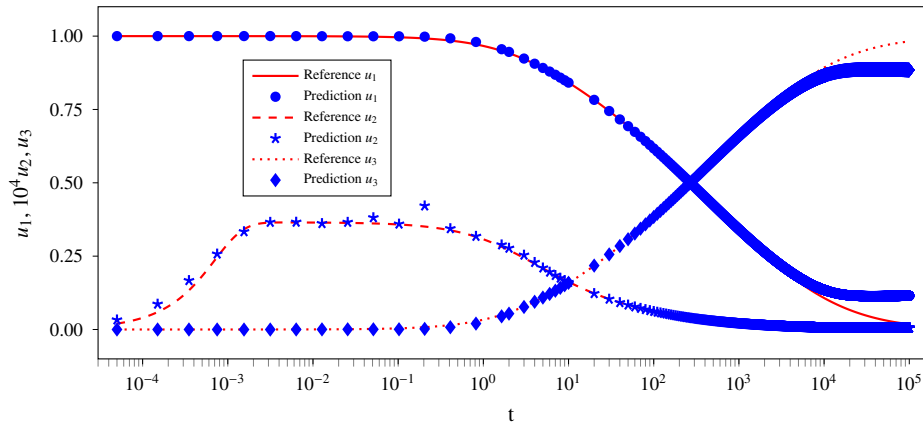
(a) Baseline method
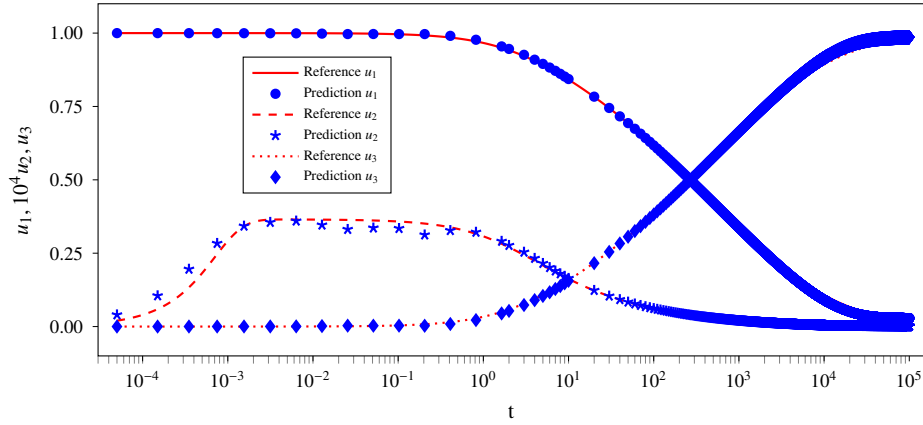
(b) LISG method

(c) GDSG method

Fig. 12: Autocatalytic chemical reaction: Predicted and reference solutions with the initial state $(1, 0, 0)$ for $t \in [0, 500000]$. The value of u_2 is multiplied by 10^4 for clear visualization.

$\Delta = 1$. After that, the large-scale model is used for the second-stage prediction from $t = 10$ to $t = 10^5$, with the time stepsize fixed as $\Delta = 10$. The numerical solutions of the GDSG method agree well with the reference solutions in the entire long-term prediction, being more accurate than those predicted by the baseline and LISG methods. It is worth mentioning that the trained models, although resembling explicit algorithms, do not suffer from the standard time step

23

restriction for such highly stiff equations.

5.1.5. ODE example 5: Glycolytic oscillator system

The Glycolytic oscillator system describes the complicated nonlinear dynamics for the concentrations of seven biochemical species [13, 50]. Its true governing equations are given by

$$
\begin{cases}
\dfrac{du_1}{dt} = J_0 - \dfrac{k_1 u_1 u_6}{1 + (u_6/K_1)^q}, \\[2mm]
\dfrac{du_2}{dt} = 2\dfrac{k_1 u_1 u_6}{1 + (u_6/K_1)^q} - k_2 u_2 (N - u_5) - k_6 u_2 u_5, \\[2mm]
\dfrac{du_3}{dt} = k_2 u_2 (N - u_5) - k_3 u_3 (A - u_6), \\[2mm]
\dfrac{du_4}{dt} = k_3 u_3 (A - u_6) - k_4 u_4 u_5 - \kappa(u_4 - u_7), \\[2mm]
\dfrac{du_5}{dt} = k_2 u_2 (N - u_5) - k_4 u_4 u_5 - k_6 u_2 u_5, \\[2mm]
\dfrac{du_6}{dt} = -2\dfrac{k_1 u_1 u_6}{1 + (u_6/K_1)^q} + 2k_3 u_3 (A - u_6) - k_5 u_6, \\[2mm]
\dfrac{du_7}{dt} = \psi\kappa(u_4 - u_7) - k u_7,
\end{cases}
\tag{46}
$$

where the parameters are taken from [50] and listed in Table 2. The training data consist of $4,000$ bursts of short trajectories with two forward time steps $\{\Delta_{1,j}, \Delta_{2,j}\}_{j=1}^{4000}$ randomly sampled from the interval $[0.05, 0.15]$ and the initial states of the trajectories randomly sampled from the domain $D = [0.15, 1.6] \times [0.19, 2.16] \times [0.04, 0.2] \times [0.1, 0.35] \times [0.08, 0.3] \times [0.14, 2.67] \times [0.05, 0.1]$.

Table 2: The values of parameters in the ODE system (46).

J_0	k_1	k_2	k_3	k_4	k_5	k_6	k	κ	q	K_1	ψ	N	A
2.5	100	6	16	100	1.28	12	1.8	13	4	0.52	0.1	1	4

In order to capture the complicated high-dimensional dynamics, we adopt a deep multi-step recursive OSG-Net with 4 blocks, and each block has 3 hidden layers with the equal width of 40 neurons. The network is trained for up to $100,000$ epochs with a batch size of 90. The parameters in the loss function of the GDSG method are set as $\lambda = 1$ and $Q = 5$. Once the models are trained satisfactorily, we conduct predictions and evaluate the prediction errors on 100 test trajectory data with forward steps $M = 50$. The average prediction errors and the standard deviation are shown in Table 3, from which we see the advantages of the proposed GDSG method in both accuracy and robustness. Figure 13 presents the prediction results of the GDSG method for the trajectory starting from the initial state $(0.2, 2.0, 0.054, 0.237, 0.152, 2.167, 0.07)$. One can observe the excellent agreement between the predicted and reference solutions.

Table 3: Glycolytic oscillator: Average prediction error $\overline{\mathcal{E}}$ on the test set and the standard deviation σ of prediction errors.

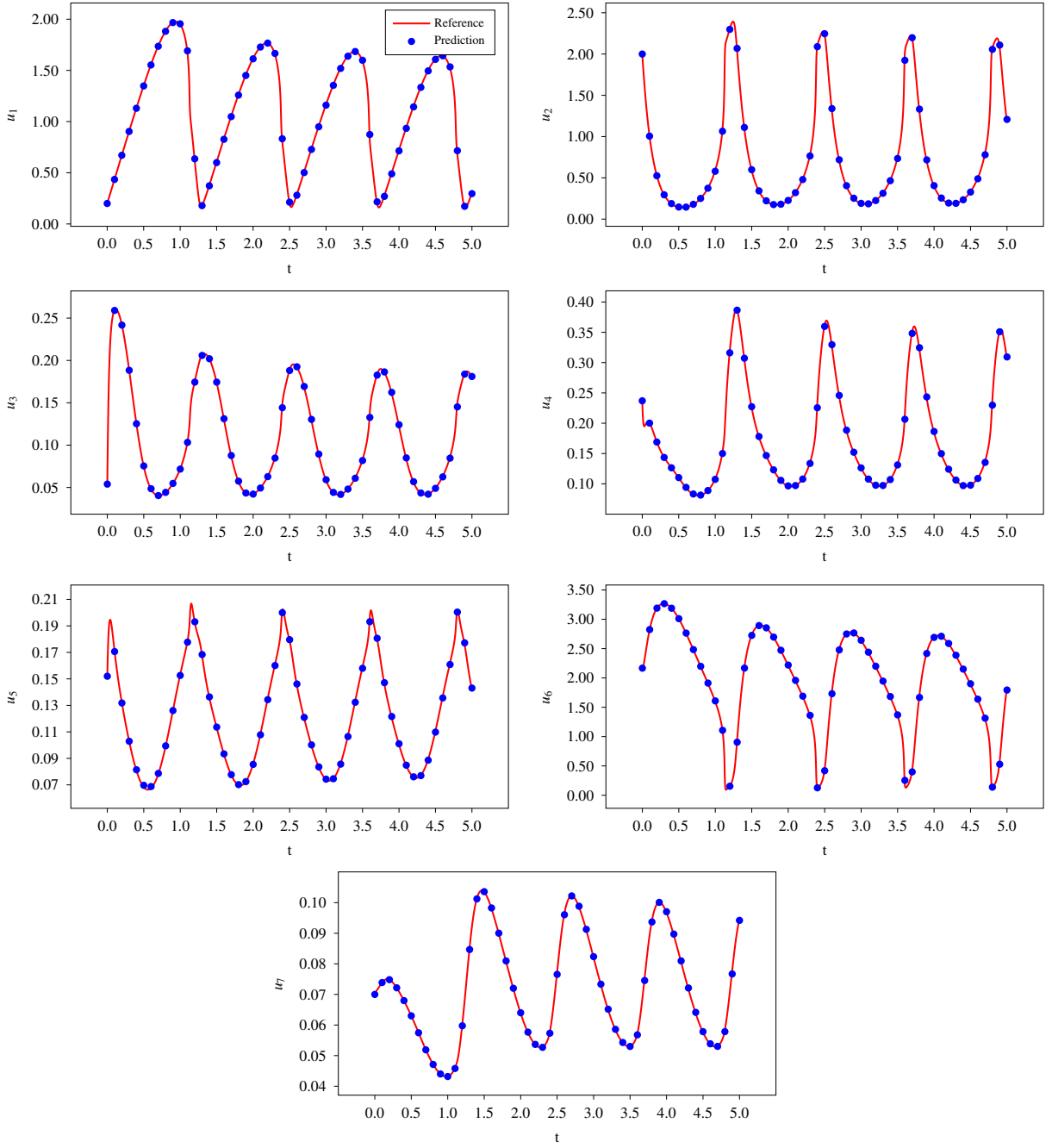|	Baseline	LISG	GDSG
Prediction error $\overline{\mathcal{E}}$	0.04439	0.0216	$\mathbf{8.138 \times 10^{-3}}$
Standard deviation σ	0.0259	0.0132	$\mathbf{4.94 \times 10^{-3}}$

Fig. 13: Glycolytic oscillator: Reference solution and predicted solution by the GDSG method. The initial state is $(0.2, 2.0, 0.054, 0.237, 0.152, 2.167, 0.07)$.

5.2. Numerical experiments on PDEs

In this section, we present several numerical experiments on a wide variety of PDEs.

5.2.1. PDE example 1: Advection equation

This example considers a 1D advection equation with periodic boundary condition:

$$\begin{cases} \partial_t u + \partial_x u = 0, & (x,t) \in (0, 2\pi) \times \mathbb{R}^+ \\ u(0,t) = u(2\pi, t), & t \geq 0. \end{cases} \tag{47}$$

We learn the evolution operators via the Deep-OSG approach in Fourier modal space. As in [30], the finite-dimensional approximation space is taken as $\mathbb{V}_7 = \text{span}\{1, \cos(x), \sin(x), \cos(2x), \sin(2x), \cos(3x), \sin(3x)\}$. The training data consist of $J = 1,000$ bursts of short "trajectories" with two forward time stepsizes $\{\Delta_{1,j}, \Delta_{2,j}\}_{j=1}^{J}$ randomly sampled in the interval $[0.05, 0.15]$. The initial conditions of the trajectories are generated in $\mathbb{V}_7$ with the Fourier coefficients randomly sampled from the domain $D = [-0.8, 0.8]^3 \times [-0.2, 0.2]^2 \times [-0.03, 0.03]^2$ in modal space by using uniform distribution. It is worth noting that the size of our dataset is much smaller than that used in [30], where $80,000$ data pairs were employed for training. Our numerical experiments indicate that the proposed Deep-OSG approach is quite suitable for learning tasks with limited data.

For neural network modeling, we use the multi-step recursive OSG-Net architecture. In order to study the effect of the number of OSG-Net blocks, we adopt four recursive OSG-Nets with 1, 2, 3, and 4 blocks, respectively. Each OSG-Net block contains 3 hidden fully-connected layers of equal width of 20 neurons. The networks are trained for up to $10,000$ epochs with a batch size of 30. We set $\lambda = 1$ and $Q = 5$ in the loss function of the GDSG method. After training the networks satisfactorily, we conduct predictions and evaluate the prediction errors on 100 test trajectory data with forward steps $M = 200$. The average relative prediction errors for different network architectures are compared in Figure 14 for the baseline, LISG and GDSG methods. As we can see, the errors decrease if more OSG-Net blocks are used.
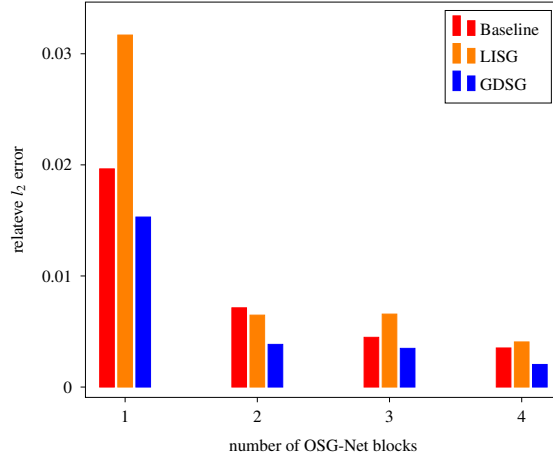

Fig. 14: Advection equation: Average prediction errors $\overline{\mathcal{E}}$ for the multi-step recursive OSG-Net with different numbers of blocks.

To validate the model, we take an initial condition $u(x, 0) = \frac{1}{2}\exp(\sin(x))$ outside the approximation space $\mathbb{V}_7$, and conduct simulations in the form (39) using the trained model given by the GDSG method with 4 blocks. In Figure 15, the solution prediction of the trained model at $t = 10$ and $t = 20$ is plotted, along with the true solution for reference. One can observe that the network model produces accurate prediction results. To further validate the prediction accuracy, we also present in Figure 16 the evolution of the learned expansion coefficients v_j, $1 \leq j \leq 7$. For comparison, the optimal Fourier coefficients obtained by the orthogonal projection of the true solution onto $\mathbb{V}_7$ are also plotted. We see excellent agreement between the predicted and true solutions.

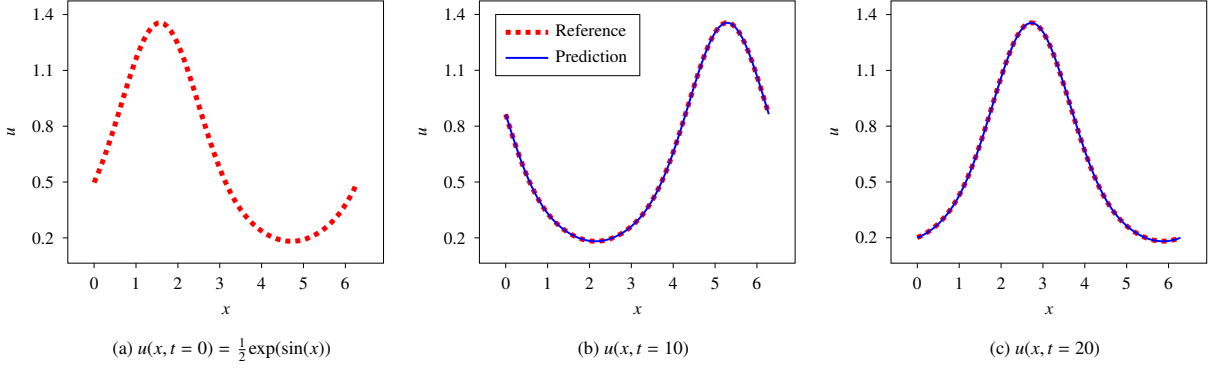(a) $u(x, t = 0) = \frac{1}{2}\exp(\sin(x))$ (b) $u(x, t = 10)$ (c) $u(x, t = 20)$

Fig. 15: Advection equation: Comparison of the true solution and the learned model solution at $t = 10$ and $t = 20$ given by the GDSG method with 4 OSG-Net blocks.

5.2.2. PDE example 2: Viscous Burgers' equation

We consider the viscous Burgers' equation with Dirichlet boundary condition:

$$
\begin{cases}
\partial_t u + \partial_x \left(\dfrac{u^2}{2}\right) = \dfrac{1}{10}\partial_{xx}u, & (x, t) \in (-\pi, \pi) \times \mathbb{R}^+, \\
u(-\pi, t) = u(\pi, t) = 0, & t \geq 0.
\end{cases}
\tag{48}
$$

In this example, the evolution operators are also learned in Fourier modal space. Following [30], the finite-dimensional approximation space is taken as $\mathbb{V}_9 = \text{span}\{\sin(ix)\}_{i=1}^9$. The training data consist of $J = 2,000$ bursts of short "trajectories" with two forward time stepsizes $\{\Delta_{1,j}, \Delta_{2,j}\}_{j=1}^J$ randomly sampled in the interval $[0.025, 0.075]$. The initial conditions of the trajectories are generated in $\mathbb{V}_9$ with the Fourier coefficients randomly sampled from the domain $D = [-1.5, 1.5] \times [-0.5, 0.5] \times [-0.2, 0.2]^2 \times [-0.1, 0.1]^2 \times [-0.05, 0.05]^2 \times [-0.02, 0.02]$ in modal space by using uniform distribution. It is worth noting that the size of our dataset is much smaller than that employed in [30], where $500,000$ data pairs were employed for training.

We adopt a deep multi-step recursive OSG-Net with 4 blocks, each of which contains 3 hidden layers of equal width of 30 neurons. The parameters in the GDSG method are set as $\lambda = 2$ and $Q = 5$. We train the network for up to $20,000$ epochs with a batch size of 90. We validate the trained model on 100 test trajectories with forward steps $M = 80$. Table 4 displays the average relative errors and the standard deviation. We observe the superior performance of the GDSG method over the LISG and baseline methods. We also employ $u(x, 0) = -\sin(x)$ as the initial condition and predict the solution at $t = 2$ and $t = 4$ by using the trained model of the GDSG method; see Figure 17. It is seen that the predicted solution preserves the symmetry about $x = 0$ and agrees well with the reference solution.

Table 4: Viscous Burgers' equation - Average prediction error $\overline{\mathcal{E}}$ on the test set and the standard deviation σ of prediction error.

	Baseline	LISG	GDSG
Prediction error $\overline{\mathcal{E}}$	0.5235	5.653×10^{-2}	$\mathbf{2.648 \times 10^{-2}}$
Standard deviation σ	0.261	2.04×10^{-3}	$\mathbf{7.36 \times 10^{-4}}$

5.2.3. PDE example 3: Inviscid Burgers' equation

In this example, we consider the inviscid Burgers' equation with periodic boundary condition:

$$
\begin{cases}
\partial_t u + \partial_x \left(\dfrac{u^2}{2}\right) = 0, & (x, t) \in (-\pi, \pi) \times \mathbb{R}^+, \\
u(-\pi, t) = u(\pi, t), & t \in \mathbb{R}^+.
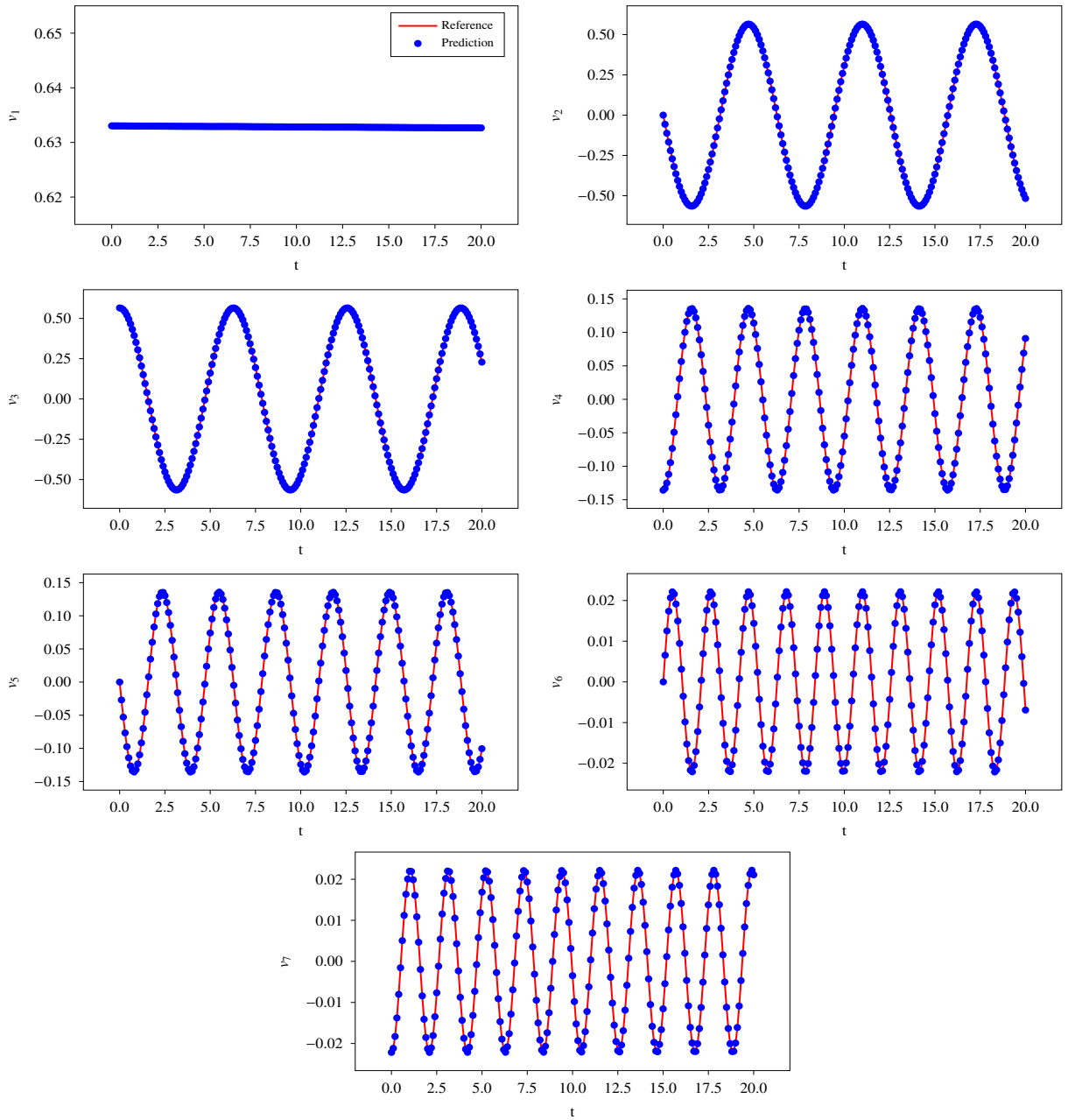\end{cases}
\tag{49}
$$

27

Fig. 16: Advection equation: Evolution of the expansion Fourier coefficients for the projection of the true solution and the learned model solution given by the GDSG method with 4 OSG-Net blocks.

This is a challenging problem due to the hyperbolic nature of the system (49), as its solution can produce shocks over time even if the initial condition is smooth. The training data is generated by solving the true PDE (49) using a ninth-order finite difference weighted essentially non-oscillatory (WENO) scheme with the fourth-order Runge–Kutta time discretization, starting from 800 different initial conditions in the following form

$$u(x,0) = a_0 + \sum_{n=1}^{10} (a_n \cos(nx) + b_n \sin(nx)),$$

(a) $u(x, 0) = -\sin(x)$ (b) $u(x, t = 2)$ (c) $u(x, t = 4)$
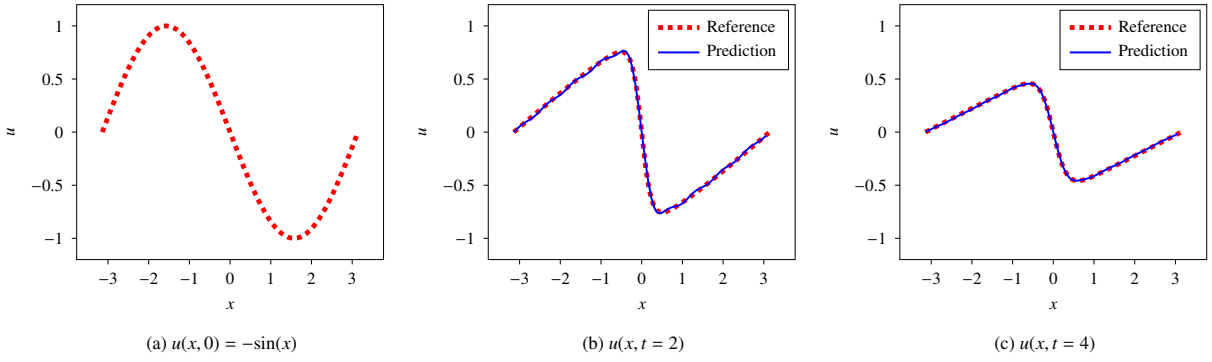
Fig. 17: Viscous Burgers' equation: Comparison of the true solution and the learned model solution at $t = 2$ and $t = 4$ given by the GDSG method.

where the Fourier coefficients $\{a_n, b_n\}$ are randomly sampled by uniform distributions on pre-defined intervals, with $a_0 \sim U[-\frac{1}{2}, \frac{1}{2}]$ and $a_n, b_n \sim U[-\frac{1}{n}, \frac{1}{n}]$. Starting from each initial condition, we collect 10 snapshot data over time with the stepsizes randomly drawn from the interval $[0.05, 0.15]$. The data are sampled on a uniform mesh of 64 nodal points.

Note that our dataset only contains smooth solutions, and its size is much smaller than that used in [31], where $20,000$ trajectory data were used with $10,000$ data containing discontinuous solutions.

In this example, we conduct the learning task of the evolution operator in nodal space, on the mesh of 64 uniform girds. We employ the OSG-Net with the special deep neural network proposed in [31] as the basic block. The parameters in the loss function of the GDSG method are set as $\lambda = 2$ and $Q = 5$. The network is trained for up to $5,000$ epochs with a batch size equal to 90. We then validate the trained models of the baseline, LISG, and GDSG methods on 100 test trajectories with $M = 20$. The average prediction errors $\overline{\mathcal{E}}$ and the standard deviation σ are presented in Table 5. We see that the LISG and GDSG methods produce more accurate and robust predictions than the baseline, while the GDSG method outperforms the LISG method. We also use an initial condition $u(x, 0) = -\sin(x)$ and conduct simulations using the trained model of the GDSG method for time up to $t = 2$. The predicted solutions at several different time instances are plotted in Figure 18, along with the reference solution. As we can see, the solution starts to develop shock at $x = 0$ when $t \geq 1$, and the prediction results agree well with the reference solution. It is worth noting that our model is trained to learn the evolution operator based on only smooth solution data and without any knowledge of the true equation. Interestingly, the learned evolution operator is able to produce shock structure developed over time.

Table 5: Inviscid Burgers' equation: Average prediction error $\overline{\mathcal{E}}$ on the test set and the standard deviation σ of prediction errors.

	Baseline	LISG	GDSG
Prediction error $\overline{\mathcal{E}}$	3.024×10^{-2}	2.957×10^{-2}	$\mathbf{2.433 \times 10^{-2}}$
Standard deviation σ	0.0118	8.62×10^{-3}	$\mathbf{7.31 \times 10^{-3}}$

(a) $u(x, t = 0.5)$

(b) $u(x, t = 1.0)$

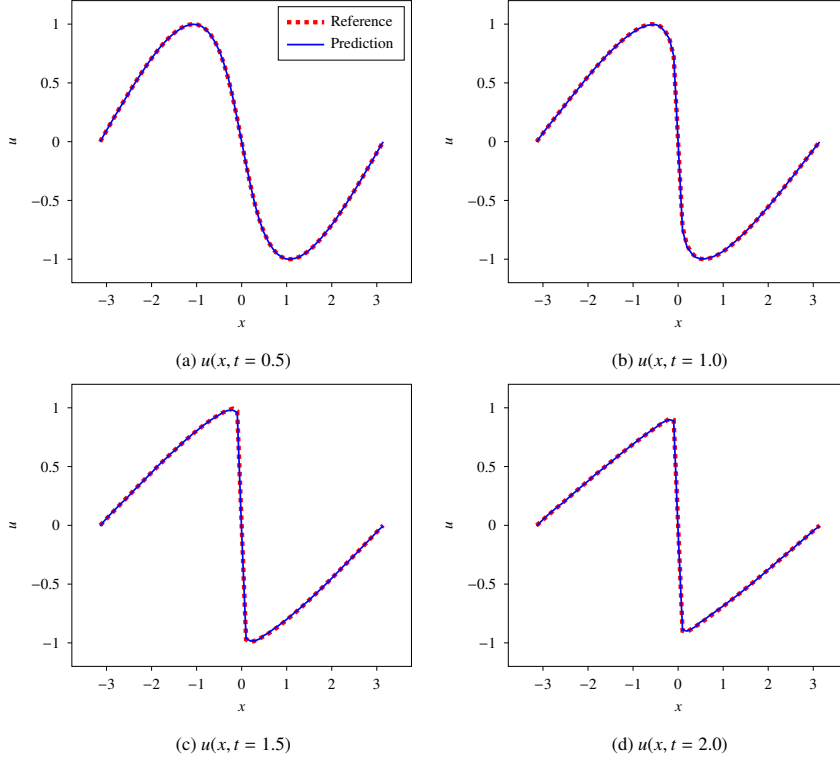(c) $u(x, t = 1.5)$

(d) $u(x, t = 2.0)$

Fig. 18: Inviscid Burgers' equation: Comparison of the reference solution and the learned model solution given by the GDSG method at $t = 0.5, 1.0, 1.5, 2.0$.

5.2.4. PDE example 4: Two-dimensional convection-diffusion equation

To demonstrate the applicability of our Deep-OSG approach for multidimensional problems, we consider a two-dimensional convection-diffusion equation [30] with periodic boundary conditions:

$$
\begin{cases}
\partial_t u + \alpha_1 \partial_x u + \alpha_2 \partial_y u = \sigma_1 \partial_{xx} u + \sigma_2 \partial_{yy} u, & (x, y, t) \in (-\pi, \pi) \times (-\pi, \pi) \times \mathbb{R}^+, \\
u(-\pi, y, t) = u(\pi, y, t), & (y, t) \in (-\pi, \pi) \times \mathbb{R}^+, \\
\partial_x u(-\pi, y, t) = \partial_x u(\pi, y, t), & (y, t) \in (-\pi, \pi) \times \mathbb{R}^+, \\
u(x, -\pi, t) = u(x, \pi, t), & (x, t) \in (-\pi, \pi) \times \mathbb{R}^+, \\
\partial_y u(x, -\pi, t) = \partial_y u(x, \pi, t), & (x, t) \in (-\pi, \pi) \times \mathbb{R}^+,
\end{cases}
\tag{50}
$$

where the parameters are taken as $(\alpha_1, \alpha_2) = (1, 0.7)$ and $(\sigma_1, \sigma_2) = (0.1, 0.16)$.

The learning task of this problem is conducted in modal space, with the finite-dimensional approximation space $\mathbb{V}_n$ taken as the span of $n = 25$ basis functions as in [30].

The training data consist of $J = 2,000$ bursts of short "trajectories" with two forward time stepsizes $\{\Delta_{1,j}, \Delta_{2,j}\}_{j=1}^{J}$ randomly sampled in the interval $[0.05, 0.15]$. Our dataset is much smaller than that employed in [30], where $1,000,000$ data pairs were used for training. For neural network modeling, we adopt a deep multi-step recursive OSG-Net with 3 blocks, and each block contains 3 hidden layers of equal width of 40 neurons. The parameters in the loss function of the GDSG method are set as $\lambda = 2$ and $Q = 5$. After training the network for up to 500 epochs with a batch size of 90, we validate the trained models on 100 test trajectories with $M = 30$. The results of the baseline, LISG, and GDSG methods are listed and compared in Table 6. Again, we observe that the model obtained by the GDSG and LISG methods produce more accurate and robust predictions than the baseline method, while the performance of the GDSG method is the best. For further validation, we take an initial condition from the test set and present the contours of the prediction solution of the GDSG method at $t = 1.5$ and $t = 3$ in Figure 19, along with the

true solution for comparison. One can see good agreement between the predicted and true solutions.
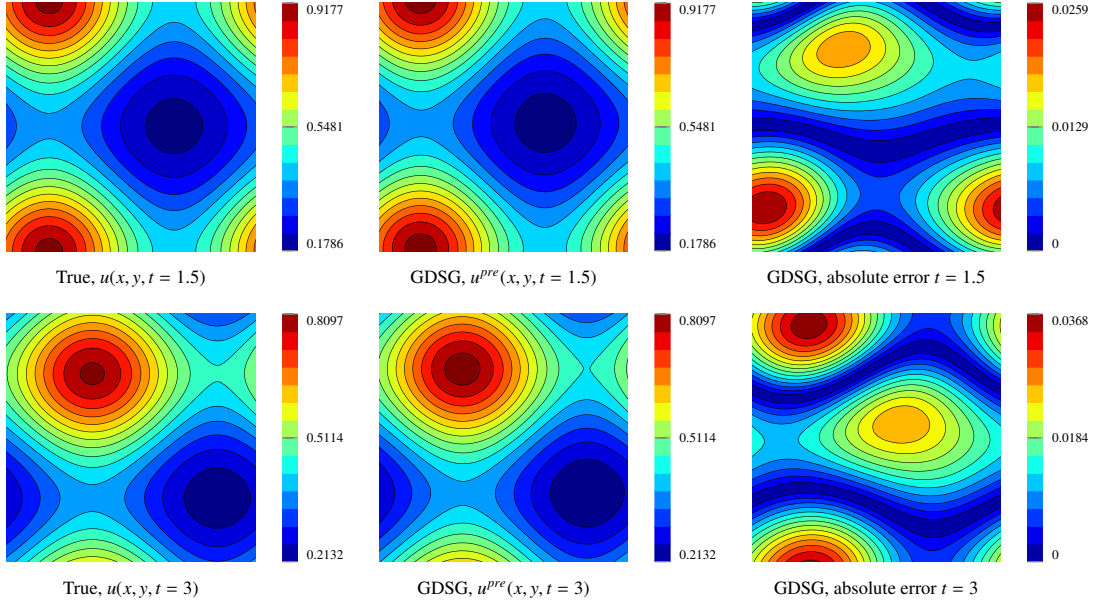

Fig. 19: Two-dimensional convection-diffusion equation: Contour plots of the solutions and errors at $t = 1.5$ and $t = 3$. Left: true solution; middle: learned model solution given by the GDSG method; right: absolute error in the learned model solution.

Table 6: Two-dimensional convection-diffusion equation: Average prediction error $\overline{\mathcal{E}}$ and the standard deviation σ of prediction errors.

	Baseline	LISG	GDSG
Prediction error $\overline{\mathcal{E}}$	1.063×10^{-2}	1.104×10^{-2}	$\mathbf{9.093 \times 10^{-3}}$
Standard deviation σ	1.42×10^{-3}	7.28×10^{-4}	$\mathbf{2.68 \times 10^{-4}}$

5.2.5. PDE example 5: Two-dimensional Navier–Stokes equations

In the last example, we consider the two-dimensional incompressible Navier–Stokes equations:

$$
\begin{cases}
\partial_t \omega(\mathbf{x}, t) + \mathbf{u}(\mathbf{x}, t) \cdot \nabla \omega(\mathbf{x}, t) = \nu \Delta \omega(\mathbf{x}, t) + f(\mathbf{x}), & \mathbf{x} \in (0, 1)^2, t > 0, \\
\nabla \cdot \mathbf{u}(\mathbf{x}, t) = 0, & \mathbf{x} \in (0, 1)^2, t > 0, \\
\omega(\mathbf{x}, t = 0) = \omega_0(\mathbf{x}), & \mathbf{x} \in (0, 1)^2,
\end{cases}
\tag{51}
$$

where $\mathbf{x} = (x_1, x_2)$ represents the spatial coordinates, $\mathbf{u}(\mathbf{x}, t)$ is the velocity field, $\omega = \nabla \times \mathbf{u}$ is the vorticity, $\nu = 10^{-3}$ denotes the viscosity, and $f(\mathbf{x}) = 0.1(\sin(2\pi(x_1 + x_2)) + \cos(2\pi(x_1 + x_2)))$ stands for a periodic external force. All the data are generated on a 64×64 Cartesian grid. For the training data, we sample 100 different initial conditions $\omega_0(\mathbf{x}) \sim \mu$ where $\mu = N(0, 7^3(-\Delta + 49I)^{-2.5})$ with periodic boundary conditions by following [43]. For each initial condition, we collect the snapshot data at $M = 110$ time instances with the time lags randomly drawn from the interval $[0.5, 1.5]$. To reduce the impact of Gaussian initialization, we only use the last 51 snapshots as training data.

In this example, we learn the evolution operator of the vorticity ω in nodal space, on the 64×64 uniform grid. For neural network modeling, we employ the Fourier neural operator proposed in [43] as the basic block to construct our OSG-Net. The input of such an OSG-Net is a tensor with shape $2 \times 64 \times 64$. The first channel is the vorticity field $\omega_{\text{in}} \in \mathbb{R}^{64 \times 64}$, while in the second channel we repeat the time stepsize Δ at each grid point. The output tensor is

a single-channel tensor, *i.e.* the predicted vorticity field $\omega_{\text{out}} \in \mathbb{R}^{64 \times 64}$. For less memory usage and faster training, we set $Q = 1$ in the loss function of the GDSG method, while the parameter λ is set as 0.5. The OSG-Net is trained for up to $1,000$ epochs with a batch size of 20.

The trained models by the baseline, LISG, and GDSG methods are validated on a test dataset of 100 long trajectories with $M = 100$. The prediction errors $\{\mathcal{E}(t_m)\}_{m=1}^{M}$ defined by (40) are computed, and their evolution is shown in Figure 20. We see that the prediction errors of the baseline method grow very fast and finally blows up, indicating the trained model is not stable. For both the LISG and GDSG methods, the trained models perform fairly well in when $t < 50$. However, the error curve for the LISG method lifts rapidly after $t > 50$. Only the GDSG method produces a reliable model for $50 < t \leq 100$, and the relative error of its prediction at $t = 100$ remains smaller than 3%. The average prediction errors and standard deviation are further compared in Table 7 for the three methods. We clearly see the remarkable advantages of the GDSG method in both accuracy and robustness. For further validation, we take an initial condition from the test set and compare the predicted vorticity obtained by the LISG and GDSG methods in Figure 21, along with the reference solution. The corresponding absolute errors are shown in Figures 22 and 23.

We observe that the prediction results given by the LISG method become visibly unacceptable at $t = 100$, while the GDSG method still produces accurate predictions that agree well with the reference solution. All these observations further confirm the importance and remarkable benefits of embedding the semigroup property for evolution operator learning.
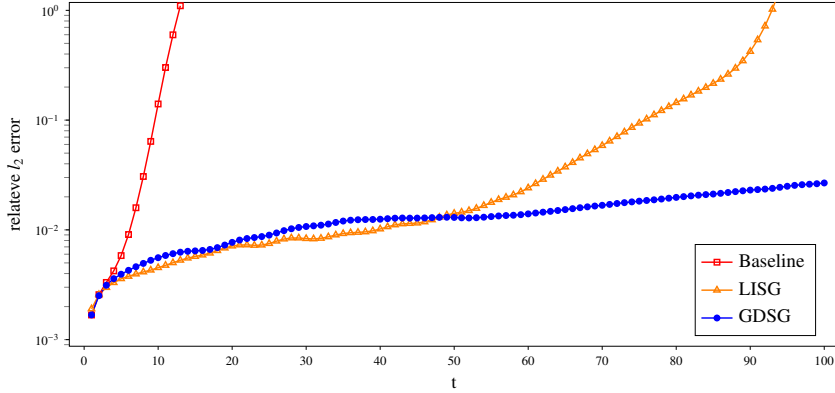

Fig. 20: Navier–Stokes equations: Evolution of the prediction errors over time. The curves of baseline and LISG methods are not shown completely as the errors blow up.

Table 7: Navier–Stokes equations: Average prediction error $\overline{\mathcal{E}}$ on the test set and the standard deviation σ of prediction errors.

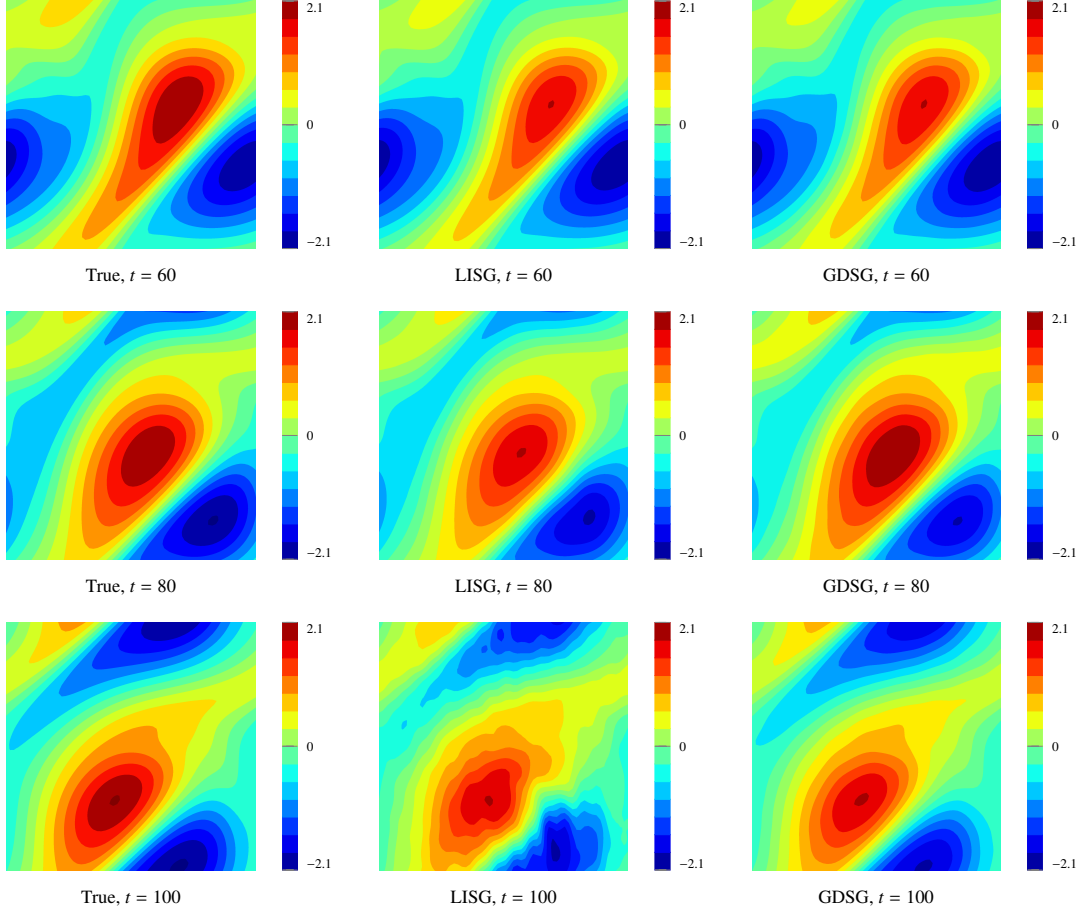|	Baseline	LISG	GDSG
Prediction error $\overline{\mathcal{E}}$	1.143×10^{31}	6.034	**0.0158**
Standard deviation σ	1.51×10^{31}	4.32×10^5	**0.0155**

Fig. 21: Navier–Stokes equations: The true and predicted vorticity fields given by the LISG and GDSG methods at $t = 60, 80, 100$.
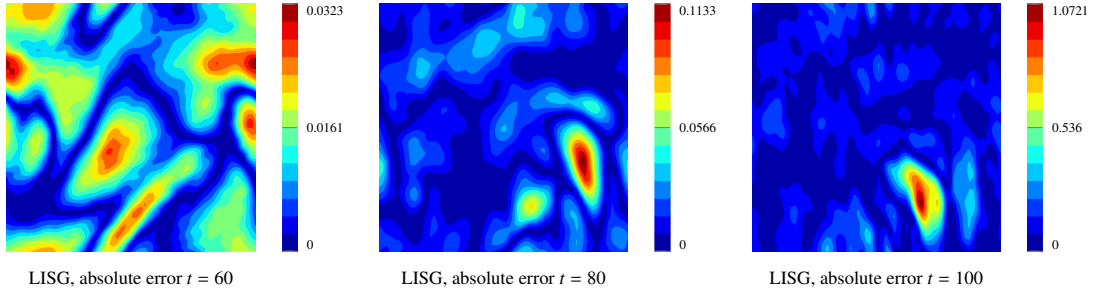

Fig. 22: Navier–Stokes equations: The absolute errors in the predicted solutions of the LISG method at $t = 60, 80, 100$.

6. Conclusions

In this paper, we have presented a framework for approximating evolution operators and modeling unknown autonomous ODE and PDE systems using time series data collected at varied time lags. Unlike the previous works [29, 30, 31] which focused on learning a single evolution operator with a fixed time step, our new framework is designed to learn a family of evolution operators with variable time steps, which constitute a semigroup for an autonomous system. The semigroup property is very crucial, as it links the system's evolutionary behaviors across varying time scales. For the first time, we have proposed an approach of embedding the semigroup property into the data-driven learning process, based on a novel neural network architecture and new loss functions. Rigorous error estimates and

33

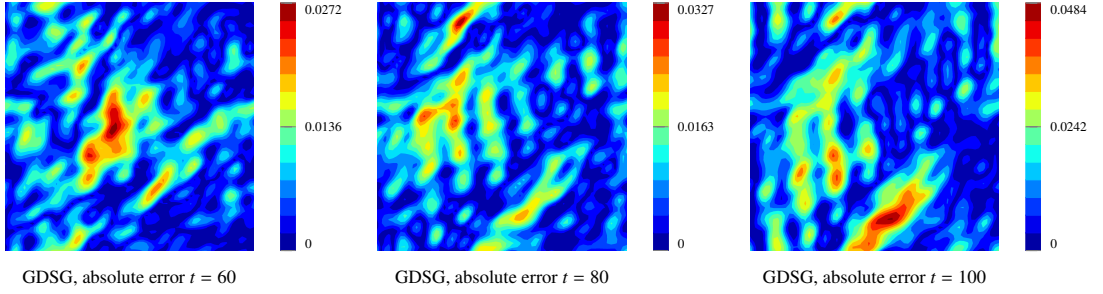| GDSG, absolute error $t = 60$ | GDSG, absolute error $t = 80$ | GDSG, absolute error $t = 100$ |

Fig. 23: Navier–Stokes equations: The absolute errors in the predicted solutions of the GDSG method at $t = 60, 80, 100$.

variance analysis have been carried out to understand the prediction accuracy and robustness of our approach. We have shown that the semigroup awareness our model significantly improves the prediction accuracy and greatly enhances the robustness and stability. Moreover, our model allows one to arbitrarily choose the time steps for prediction and ensures that the predicted results are well self-matched and consistent for different partitions of the time interval. The proposed framework is very feasible, can be combined with any suitable neural networks, and is applicable to data-driven learning of general autonomous ODEs and PDEs. We have presented extensive numerical examples, including a stiff ODE system and the complicated Navier–Stokes equations, which have shown that our approach with the embedded semigroup property produces more accurate, robust, and reliable models compared to the purely data-driven approach. Moreover, embedding the semigroup property also notably reduces the required data, slows down the error growth over time, and greatly enhances the stability for long-time prediction.

Appendix A.

This appendix provides some supplementary results concerning two helpful techniques, which are used in our numerical experiments.

Appendix A.1. Data normalization

In this work, every component(channel) of the vectors(the tensors) is normalized to $[-1, 1]$ before network training, by using their maximum and minimum values in the dataset. We choose the ODE example 1 and compare the trained model performance with and without data normalization; see Tables A.8. The results clearly justify the benefits of using data normalization.

Table A.8: Linear ODEs: Average prediction error $\overline{\mathcal{E}}$ and standard deviation σ on the test set, with and without data normaliaztion

		Baseline	LISG	GDSG
Prediction error $\overline{\mathcal{E}}$	With normalization	$\mathbf{5.558 \times 10^{-3}}$	$\mathbf{1.708 \times 10^{-3}}$	$\mathbf{7.652 \times 10^{-4}}$
	No normalization	2.179×10^{-2}	3.736×10^{-3}	4.640×10^{-3}
Standard deviation σ	With normalization	1.951×10^{-3}	$\mathbf{3.440 \times 10^{-4}}$	$\mathbf{4.932 \times 10^{-5}}$
	No normalization	$\mathbf{1.479 \times 10^{-3}}$	1.151×10^{-3}	4.200×10^{-4}

Appendix A.2. Dynamic validation

We now present a few results to justify the advantages of using dynamic validation technique, which was mentioned in Remark 8. Tables A.9 displays the results on the periodic attractor example (see section 5.1.2), which has merely 50 bursts of short trajectories in the dataset. It is seen that the dynamic validation technique enhances the performance for all the three methods.

Table A.9: Periodic attractor: Average prediction error $\overline{\mathcal{E}}$ and standard deviation σ on the test set, with and without dynamic validation.

		Baseline	LISG	GDSG
Prediction error $\overline{\mathcal{E}}$	Dynamic validation set	$\mathbf{6.705 \times 10^{-3}}$	$\mathbf{5.465 \times 10^{-3}}$	$\mathbf{5.175 \times 10^{-3}}$
	Fixed validation set	0.01315	0.01306	8.309×10^{-3}
Standard deviation σ	Dynamic validation set	$\mathbf{6.58 \times 10^{-3}}$	$\mathbf{4.34 \times 10^{-3}}$	$\mathbf{9.38 \times 10^{-4}}$
	Fixed validation set	6.93×10^{-3}	5.27×10^{-3}	1.26×10^{-3}

References

[1] J. Bongard, H. Lipson, Automated reverse engineering of nonlinear dynamical systems, Proceedings of the National Academy of Sciences 104 (2007) 9943–9948.

[2] M. Schmidt, H. Lipson, Distilling free-form natural laws from experimental data, Science 324 (2009) 81–85.

[3] S. L. Brunton, J. L. Proctor, J. N. Kutz, Discovering governing equations from data by sparse identification of nonlinear dynamical systems, Proceedings of the National Academy of Sciences 113 (2016) 3932–3937.

[4] S. H. Rudy, S. L. Brunton, J. L. Proctor, J. N. Kutz, Data-driven discovery of partial differential equations, Science Advances 3 (2017) e1602614.

[5] R. Tibshirani, Regression shrinkage and selection via the lasso, Journal of the Royal Statistical Society: Series B (Methodological) 58 (1996) 267–288.

[6] D. L. Donoho, Compressed sensing, IEEE Transactions on information theory 52 (2006) 1289–1306.

[7] E. J. Candes, J. K. Romberg, T. Tao, Stable signal recovery from incomplete and inaccurate measurements, Communications on Pure and Applied Mathematics 59 (2006) 1207–1223.

[8] H. Schaeffer, S. G. McCalla, Sparse model selection via integral terms, Physical Review E 96 (2017) 023302.

[9] H. Schaeffer, Learning partial differential equations via data discovery and sparse optimization, Proceedings of the Royal Society A: Mathematical, Physical and Engineering Sciences 473 (2017) 20160446.

[10] G. Tran, R. Ward, Exact recovery of chaotic systems from highly corrupted data, Multiscale Modeling & Simulation 15 (2017) 1108–1129.

[11] Z. Long, Y. Lu, X. Ma, B. Dong, PDE-Net: Learning PDEs from data, in: International Conference on Machine Learning, PMLR, 2018, pp. 3208–3216.

[12] M. Raissi, Deep hidden physics models: Deep learning of nonlinear partial differential equations, The Journal of Machine Learning Research 19 (2018) 932–955.

[13] M. Raissi, P. Perdikaris, G. E. Karniadakis, Multistep neural networks for data-driven discovery of nonlinear dynamical systems, arXiv preprint arXiv:1801.01236 (2018).

[14] Z. Long, Y. Lu, B. Dong, PDE-Net 2.0: Learning PDEs from data with a numeric-symbolic hybrid deep network, Journal of Computational Physics 399 (2019) 108925.

[15] M. Raissi, P. Perdikaris, G. E. Karniadakis, Physics-informed neural networks: A deep learning framework for solving forward and inverse problems involving nonlinear partial differential equations, Journal of Computational physics 378 (2019) 686–707.

[16] Y. Sun, L. Zhang, H. Schaeffer, NeuPDE: Neural network based ordinary and partial differential equations for modeling time-dependent data, in: Mathematical and Scientific Machine Learning, PMLR, 2020, pp. 352–372.

[17] Y. Chen, T. Matsubara, T. Yaguchi, Neural symplectic form: Learning Hamiltonian equations on general coordinate systems, Advances in Neural Information Processing Systems 34 (2021) 16659–16670.

[18] S. Atkinson, W. Subber, L. Wang, G. Khan, P. Hawi, R. Ghanem, Data-driven discovery of free-form governing differential equations, arXiv preprint arXiv:1910.05117 (2019).

[19] Y. Chen, Y. Luo, Q. Liu, H. Xu, D. Zhang, Symbolic genetic algorithm for discovering open-form partial differential equations (SGA-PDE), Physical Review Research 4 (2022) 023174.

[20] M. Raissi, P. Perdikaris, G. E. Karniadakis, Machine learning of linear differential equations using Gaussian processes, Journal of Computational Physics 348 (2017) 683–693.

[21] N. M. Mangan, J. N. Kutz, S. L. Brunton, J. L. Proctor, Model selection for dynamical systems via sparse regression and information criteria, Proceedings of the Royal Society A: Mathematical, Physical and Engineering Sciences 473 (2017) 20170009.

[22] S. L. Brunton, B. W. Brunton, J. L. Proctor, E. Kaiser, J. N. Kutz, Chaos as an intermittently forced linear system, Nature Communications 8 (2017) 19.

[23] K. Wu, D. Xiu, Numerical aspects for approximating governing equations using data, Journal of Computational Physics 384 (2019) 200–221.

[24] K. Wu, T. Qin, D. Xiu, Structure-preserving method for reconstructing unknown Hamiltonian systems from trajectory data, SIAM Journal on Scientific Computing 42 (2020) A3704–A3729.

[25] R. T. Keller, Q. Du, Discovery of dynamics using linear multistep methods, SIAM Journal on Numerical Analysis 59 (2021) 429–455.

[26] H. Xu, H. Chang, D. Zhang, DLGA-PDE: Discovery of PDEs with incomplete candidate library via combination of deep learning and genetic algorithm, Journal of Computational Physics 418 (2020) 109584.

[27] H. Xu, D. Zhang, J. Zeng, Deep-learning of parametric partial differential equations from sparse and noisy data, Physics of Fluids 33 (2021) 037132.

[28] H. Xu, D. Zhang, Robust discovery of partial differential equations in complex situations, Physical Review Research 3 (2021) 033270.

[29] T. Qin, K. Wu, D. Xiu, Data driven governing equations approximation using deep neural networks, Journal of Computational Physics 395 (2019) 620–635.

[30] K. Wu, D. Xiu, Data-driven deep learning of partial differential equations in modal space, Journal of Computational Physics 408 (2020) 109307.

[31] Z. Chen, V. Churchill, K. Wu, D. Xiu, Deep neural network modeling of unknown partial differential equations in nodal space, Journal of Computational Physics 449 (2022) 110782.

[32] T. Qin, Z. Chen, J. D. Jakeman, D. Xiu, Deep learning of parameterized equations with applications to uncertainty quantification, International Journal for Uncertainty Quantification 11 (2021).

[33] X. Fu, L.-B. Chang, D. Xiu, Learning reduced systems via deep neural networks with memory, Journal of Machine Learning for Modeling and Computing 1 (2020).

[34] V. Churchill, D. Xiu, Deep learning of chaotic systems from partially-observed data, Journal of Machine Learning for Modeling and Computing 3 (2022).

[35] T. Qin, Z. Chen, J. D. Jakeman, D. Xiu, Data-driven learning of nonautonomous systems, SIAM Journal on Scientific Computing 43 (2021) A1607–A1624.

[36] Z. Chen, D. Xiu, On generalized residual network for deep learning of unknown dynamical systems, Journal of Computational Physics 438 (2021) 110362.

[37] W.-H. Su, C.-S. Chou, D. Xiu, Deep learning of biological models from data: Applications to ODE models, Bulletin of Mathematical Biology 83 (2021) 1–19.

[38] L. Lu, P. Jin, G. Pang, Z. Zhang, G. E. Karniadakis, Learning nonlinear operators via DeepONet based on the universal approximation theorem of operators, Nature Machine Intelligence 3 (2021) 218–229.

[39] S. Cai, Z. Wang, L. Lu, T. A. Zaki, G. E. Karniadakis, DeepM&Mnet: Inferring the electroconvection multiphysics fields based on operator approximation by neural networks, Journal of Computational Physics 436 (2021) 110296.

[40] Z. Mao, L. Lu, O. Marxen, T. A. Zaki, G. E. Karniadakis, DeepM&Mnet for hypersonics: Predicting the coupled flow and finite-rate chemistry behind a normal shock using neural-network approximation of operators, Journal of computational physics 447 (2021) 110698.

[41] N. Kovachki, Z. Li, B. Liu, K. Azizzadenesheli, K. Bhattacharya, A. Stuart, A. Anandkumar, Neural operator: Learning maps between function spaces, arXiv preprint arXiv:2108.08481 (2021).

[42] Z. Li, N. Kovachki, K. Azizzadenesheli, B. Liu, A. Stuart, K. Bhattacharya, A. Anandkumar, Multipole graph neural operator for parametric partial differential equations, Advances in Neural Information Processing Systems 33 (2020) 6755–6766.

[43] Z. Li, N. B. Kovachki, K. Azizzadenesheli, B. liu, K. Bhattacharya, A. Stuart, A. Anandkumar, Fourier neural operator for parametric partial differential equations, in: International Conference on Learning Representations, 2021.

[44] Z. Li, N. Kovachki, K. Azizzadenesheli, B. Liu, K. Bhattacharya, A. Stuart, A. Anandkumar, Markov neural operators for learning chaotic systems, arXiv preprint arXiv:2106.06898 (2021).

[45] H. You, Y. Yu, M. D'Elia, T. Gao, S. Silling, Nonlocal kernel network (NKN): a stable and resolution-independent deep neural network, Journal of Computational Physics 469 (2022) 111536.

[46] K. He, X. Zhang, S. Ren, J. Sun, Deep residual learning for image recognition, in: Proceedings of the IEEE conference on computer vision and pattern recognition, 2016, pp. 770–778.

[47] L. N. Smith, Cyclical learning rates for training neural networks, in: 2017 IEEE Winter Conference on Applications of Computer Vision (WACV), IEEE, 2017, pp. 464–472.

[48] M. Abadi, A. Agarwal, P. Barham, E. Brevdo, Z. Chen, C. Citro, G. S. Corrado, A. Davis, J. Dean, M. Devin, S. Ghemawat, I. Goodfellow, A. Harp, G. Irving, M. Isard, Y. Jia, R. Jozefowicz, L. Kaiser, M. Kudlur, J. Levenberg, D. Mané, R. Monga, S. Moore, D. Murray, C. Olah, M. Schuster, J. Shlens, B. Steiner, I. Sutskever, K. Talwar, P. Tucker, V. Vanhoucke, V. Vasudevan, F. Viégas, O. Vinyals, P. Warden, M. Wattenberg, M. Wicke, Y. Yu, X. Zheng, TensorFlow: Large-scale machine learning on heterogeneous systems, 2015. URL: https://www.tensorflow.org/, software available from tensorflow.org.

[49] H. Robertson, The solution of a set of reaction rate equations, Numerical analysis: An introduction 178182 (1966).

[50] B. C. Daniels, I. Nemenman, Efficient inference of parsimonious phenomenological models of cellular dynamics using S-systems and alternating regression, PloS One 10 (2015) e0119821.